J. Plasma Phys. (2022), *vol*. 88, 905880104
Published by Cambridge University Press
doi:10.1017/S0022377821001318

Gamma-ray flash in the interaction of a tightly focused single-cycle ultra-intense laser pulse with a solid target

P. Hadjisolomou [1],†, T.M. Jeong[1], P. Valenta[1,2], D. Kolenaty [1], R. Versaci [1], V. Olšovcová[1], C.P. Ridgers[3] and S.V. Bulanov [1,4]

[1]ELI Beamlines Centre, Institute of Physics, Czech Academy of Sciences, Za Radnicí 835, 25241 Dolní Břežany, Czech Republic

[2]Faculty of Nuclear Sciences and Physical Engineering, Czech Technical University in Prague, Brehova 7, 11519 Prague, Czech Republic

[3]York Plasma Institute, Department of Physics, University of York, Heslington, York YO10 5DD, UK

[4]National Institutes for Quantum and Radiological Science and Technology (QST), Kansai Photon Science Institute, 8-1-7 Umemidai, Kizugawa, Kyoto 619-0215, Japan

(Received 22 September 2021; revised 6 December 2021; accepted 9 December 2021)

We employ the λ^3 regime where a near-single-cycle laser pulse is tightly focused, thus providing the highest possible intensity for the minimal energy at a certain laser power. The quantum electrodynamics processes in the course of the interaction of an ultra-intense laser with a solid target are studied via three-dimensional particle-in-cell simulations, revealing the generation of copious γ-photons and electron–positron pairs. A parametric study of the laser polarisation, target thickness and electron number density shows that a radially polarised laser provides the optimal regime for γ-photon generation. By varying the laser power in the range of 1 to 300 PW we find the scaling of the laser to γ-photon energy conversion efficiency. The laser-generated γ-photon interaction with a high-Z target is further studied using Monte Carlo simulations revealing further electron–positron pair generation and radioactive nuclide creation.

Key words: plasma simulation, intense particle beam

1. Introduction

The invention of the chirped pulse amplification (CPA) technique (Strickland & Mourou 1985) in the mid-1980s allowed the rapid growth of the laser power beyond the terawatt (TW) level. The petawatt (PW) threshold was exceeded at the end of the 20th century(Perry *et al.* 1999). Currently, the record power is for the ELI-NP 10 PW laser (Tanaka *et al.* 2020), with another 10 PW laser near completion at ELI Beamlines. Current worldwide activities concerning PW laser systems and further envisions to attain >100 PW lasers are summarized in Danson *et al.* (2019) and Li, Kato & Kawanaka (2021).

Since laser power increases by either increasing the energy or reducing the pulse duration, a single-cycle pulse was proposed (Mourou *et al.* 2002; Bulanov *et al.* 2006; Voronin *et al.* 2013). Post-compression of CPA systems leads to near-single-cycle pulses by

† Email address for correspondence: prokopis.hadjisolomou@eli-beams.eu

self-phase modulation in hollow-core fibres, although the energy is at the millijoule level (Böhle *et al.* 2014; Ouillé *et al.* 2020). A second technique producing near-single-cycle pulses is optical parametric CPA, by which a 4.5 fs, 16 TW pulse has been reported (Rivas *et al.* 2017). Reducing the pulse duration is the primary goal of ELI-ALPS, where a 17 fs, 2 PW laser is under development (Osvay *et al.* 2019). Thus, at a given laser power, reduction of the pulse duration leads to a linear reduction of the energy, consequently the minimum laser energy for a single-cycle pulse.

However, it is most desired to reach the highest laser intensity rather than power. The quadratic dependency of the intensity on the inverse of the focal spot radius points to an emphasis on a reduced focal spot. More than two decades ago, a theoretical estimation of the minimum focal spot diameter (Sales 1998) suggests a value of $4\pi^{-2}\lambda$, where λ is the laser wavelength. A vectorial diffraction approach was adopted (Richards, Wolf & Gabor 1959; April & Piché 2010) to describe a focal spot smaller than the wavelength. The benefit of the vectorial representation is that Maxwell's equations are satisfied at any point in space, and analytical expressions for the electric and magnetic field components can be calculated (April & Piché 2010; Jeong *et al.* 2015; Salamin 2015). Experimental implementation of a tight-focusing scheme by a parabola with f-number f_N (the ratio of focal length f to beam diameter D) of 0.6 claims focusing of a 45 TW laser to a focal spot of $\sim$0.8 μm in diameter, leading to an intensity of $\sim 10^{22}$ W cm^{-2} (Bahk *et al.* 2004), where a similar intensity is achieved by focusing a 0.3 PW laser using a parabola of $f_N = 1.3$ (Pirozhkov *et al.* 2017).

Apart from the usually employed linearly polarised (LP) lasers, radially polarised (RP) and azimuthally polarised (AP) lasers draw much interest of several research groups, employing multi-PW lasers for electron (Salamin 2010*a*; Payeur *et al.* 2012) and proton/ion (Salamin 2010*a*; Li *et al.* 2012; Ghotra & Kant 2015) acceleration. Let us define the laser propagation direction to be along $\hat{\boldsymbol{x}}$. In cylindrical coordinates, a RP plane wave satisfies $E_r\hat{\boldsymbol{r}} = cB_\phi\hat{\boldsymbol{\phi}}$ everywhere, where $E_r\hat{\boldsymbol{r}}$ is the radial electric field component, $B_\phi\hat{\boldsymbol{\phi}}$ is the azimuthal magnetic field component and c is the speed of light in vacuum. For an AP laser, the electric and magnetic field components are interchanged. However, under tight-focusing conditions the relation $E_r\hat{\boldsymbol{r}} = cB_\phi\hat{\boldsymbol{\phi}}$ breaks down due to the appearance of a longitudinal electric field component $E_x\hat{\boldsymbol{x}}$ for a RP laser and a longitudinal magnetic field component $B_x\hat{\boldsymbol{x}}$ for an AP laser (Salamin 2006, 2010*b*; Jeong *et al.* 2018). Compared with LP lasers, both RP and AP lasers were found experimentally to give a smaller focal spot (Dorn, Quabis & Leuchs 2003; Cheng *et al.* 2015), in agreement with the elongated electric field distribution for a LP laser (Jeong *et al.* 2018).

When the concept of a single-cycle laser is combined with the tight-focusing technique, then the λ^3 regime is obtained, where for a certain laser power one can use minimal energy to achieve the highest intensity (Mourou *et al.* 2002). The λ^3 pulses offer potential unique capabilities for atomic and molecular physics (Brabec & Krausz 2000), electron–laser collisions (Tamburini, Keitel & Di Piazza 2014*b*) and relativistic nanophotonics (Cardenas *et al.* 2019), where such pulses may open up the investigation of a qualitatively new regime. If the λ^3 regime is applied to a 100 PW laser, then an intensity exceeding 10^{25} W cm^{-2} will be achieved. For comparison, a record intensity of $\sim 10^{23}$ W cm^{-2} has been recently reported for a $\sim$4 PW laser (Yoon *et al.* 2021). Although generation of λ^3 pulses by optical means is challenging, this can also be realised by plasma-based techniques (Mourou *et al.* 2014; Tamburini *et al.* 2014*a*). Notably, the self-generation of such pulses has been observed in three-dimensional simulations during the interaction of a laser pulse with a foil target (Tamburini *et al.* 2012).

The ultra-intense λ^3 regime is capable of providing a plethora of particles, such as γ-photons, leptons (electrons (e^-) and positrons (e^+)) and hadrons (protons (p^+) and/or

https://doi.org/10.1017/S0022377821001318 Published online by Cambridge University Press

heavy ions (i^+)) (Mourou, Tajima & Bulanov 2006). Although γ-photons are achievable even by near-PW-class lasers, high laser to γ-photon energy conversion efficiency, κ_γ, is important for applications in photonuclear reactions (Nedorezov, Turinge & Shatunov 2004), astrophysical studies (Rees & Mészáros 1992; Bulanov *et al.* 2015; Philippov & Spitkovsky 2018; Aharonian *et al.* 2021) and study of the extremely high energy density of materials science (Eliasson & Liu 2013).

At laser intensities of $\sim 10^{24}$ W cm^{-2} the multi-photon Compton scattering process dominates the γ-photon emission (Ridgers *et al.* 2013; Lezhnin *et al.* 2018; Younis *et al.* 2021). During that process, a hot electron/positron is scattered after collision with the incident laser field, its velocity and direction values change and a scattered γ-photon is produced. The process is summarised as $e^\pm + N\omega_l \rightarrow e^\pm + \omega_\gamma$, where ω_l is the central laser frequency, ω_γ is the scattered γ-photon frequency and $N \gg 1$ is the number of laser photons lost.

The Schwinger field represents the field required for the vacuum to break into an e^-–e^+ pair, and it is given by $E_S = m_e^2 c^3/(e\hbar) \approx 1.3 \times 10^{18}$ V m^{-1}, where m_e is the electron rest mass, $\hbar$ is the reduced Planck constant and e is the elementary charge (Berestetskii, Lifshitz & Pitaevskii 1982). The probability that a γ-photon will be emitted through multi-photon Compton scattering depends on the parameter (Ritus 1970)

$$\chi_e = \sqrt{\left(\gamma_e \frac{\boldsymbol{E}}{E_S} + \frac{\boldsymbol{p}}{m_e} \times \frac{\boldsymbol{B}}{E_S}\right)^2 - \left(\frac{\boldsymbol{p}}{m_e c} \cdot \frac{\boldsymbol{E}}{E_S}\right)^2}, \tag{1.1}$$

where γ_e is the electron/positron Lorentz factor of momentum $\boldsymbol{p}$ prior scattering and $\boldsymbol{B}$ and $\boldsymbol{E}$ are the magnetic and electric fields at the position of the electron. For high κ_γ the condition $\chi_e \gg 1$ must be met (Nakamura *et al.* 2012; Ridgers *et al.* 2012). Although the emission model used (Ridgers *et al.* 2013) breaks down for $\alpha \chi_e^{2/3} > 1$ (Ritus 1970; Ilderton 2019; Narozhny 1979; Podszus & Di Piazza 2019), where $\alpha = e^2/(4\pi\varepsilon_0 \hbar c)$ is the fine structure constant and ε_0 is the vacuum permittivity, it requires laser intensities significantly higher than those used in the present work.

The e^-–e^+ pair generation mechanism discussed in § 3 is the multi-photon Breit–Wheeler process (Ehlotzky, Krajewska & Kamiński 2009), summarised as $\omega_\gamma + N\omega_l \rightarrow e^- + e^+$. Here, a large number of laser photons interact with a high-energy γ-photon generated earlier through multi-photon Compton scattering, then generatinh an e^-–e^+ pair. The probability of a γ-photon producing a pair is governed by the parameter (Ritus 1970)

$$\chi_\gamma = \frac{\hbar\omega_l}{m_e c^2} \sqrt{\left(\frac{\boldsymbol{E}}{E_S} + c\hat{\boldsymbol{p}} \times \frac{\boldsymbol{B}}{E_S}\right)^2 - \left(\hat{\boldsymbol{p}} \cdot \frac{\boldsymbol{E}}{E_S}\right)^2}, \tag{1.2}$$

where $\hat{\boldsymbol{p}}$ is the unit vector of the γ-photon momentum.

The high fields available from multi-PW lasers have attracted interest in γ-photon generation. An electron co-propagating with the laser field produces neither γ-photons nor e–e^+ pairs due to the opposite contribution of the electric and magnetic terms in (1.1). However, in a realistic laser–foil experiment scenario the laser field is reflected on the foil front surface, changing its orientation and therefore enabling generation of γ-photons (Zhidkov *et al.* 2002; Koga, Esirkepov & Bulanov 2005; Gu *et al.* 2018). Another early approach toincreasing the γ-photon yield suggested the use of two counter-propagating pulses (Bell & Kirk 2008; Kirk, Bell & Arka 2009; Luo *et al.* 2015; Grismayer *et al.* 2016). This scheme was later generalised in the use of multiple laser beams (Vranic *et al.* 2016; Gong *et al.* 2017). The geometry of the target itself was also proven to be crucial, as

https://doi.org/10.1017/S0022377821001318 Published online by Cambridge University Press

the formation of a pre-plasma enhanced γ-photon formation (Lezhnin *et al.* 2018; Wang *et al.* 2020*b*). Other schemes employing microfabrication of targets taking advantage of the reflected laser field have also been investigated (Ji, Snyder & Shen 2019; Zhang *et al.* 2021). In addition to the all-optical approach, the combination of a sub-PW laser beam with high-energy electrons has been considered (Magnusson *et al.* 2019).

The theoretical framework for the absorption of the energy of a plane wave by electrons and ions of a foil target is described byVshivkov *et al.* (1998), although ignoring the energy share of generated γ-photons and consequently the effect of e^-–e^+ pairs. In (17) of Vshivkov *et al.* (1998), the target thickness, l, is connected to the electron number density, n_e, through

$$\epsilon_0 = \frac{\pi n_e l}{n_{cr}\lambda}, \tag{1.3}$$

where ϵ_0 is the normalised areal density and $n_{cr} = \varepsilon_0 m_e \omega^2/e^2$ is the critical electron number density. The optimum condition for coupling the plane wave to the target is obtained for $\epsilon_0 = a_0$, where $a_0 = eE/(m_e c\omega_l)$ is the dimensionless amplitude. For $\epsilon_0 \ll a_0$, relativistic transparency of the target results in weak coupling of the laser to the target, whilst for $\epsilon_0 \gg a_0$, the laser field is strongly reflected by the target front surface.

Equations (32) and (33) of Vshivkov *et al.* (1998) give the ratio of the reflected (at an angle θ_0 with the target normal) to incident wave amplitude (complex reflectivity) for an s-polarised laser, $r^s = \varepsilon_0/[\mathrm{i}\cos(\theta_0) + \varepsilon_0]$, and a p-polarised laser, $r^p = \varepsilon_0\cos(\theta_0)/[\mathrm{i} + \varepsilon_0\cos(\theta_0)]$, respectively. In an AP laser, E_x is always zero; in contrast, in a RP laser, E_x increases by reducing the f-number and dominates in the tight-focusing scheme. Therefore, the electric field vectors are oscillating longitudinally and transversely with respect to the target surface for normally incident ($\theta_0 = 0^\circ$) AP and RP lasers, respectively. Therefore, there is a qualitative analogy of the electric field oscillation direction of *s*-polarised and *p*-polarised lasers incident at $\theta_0 = 90^\circ$ with AP and RP lasers incident at $\theta_0 = 0^\circ$. As a result, for the tight-focusing scheme, an AP laser is reflected stronger than a RP laser. Up to this point, we have discussed the physical processes enabling us to study the interaction of an ultra-relativistic λ^3 laser with a solid target via particle-in-cell (PIC) simulations.

One aspect not addressed in PIC simulation studies is the further interactions of multi-MeV-energy particles with the surrounding material, either the vacuum chamber itself or a secondary target. Particle-in-cell-produced particles generate electrons through ionisation (Landau 1944) but also e^-–e^+ pairs through pair production in the Coulomb field of nuclei (Bethe & Heitler 1934) and/or atomic electrons (Wheeler & Lamb 1939). Post-PIC γ-photons may result from ionisation, e^-–e^+ pair production, Bremsstrahlung emission (Koch & Motz 1959; Aichelin 1991), photonuclear reactions (Compton 1923), nuclear interactions with heavy ions (Aichelin 1991), Rayleigh and/or Compton scattering (Compton 1923) or any combination thereof.

Furthermore, neutrons, protons, ions and nuclides are produced through photonuclear reactions (Hayward 1970), electronuclear reactions (Budnev *et al.* 1975) and nuclear interactions with heavy ions (Aichelin 1991). These interactions are simulated by the Monte Carlo (MC) particle transport code FLUKA (Böhlen *et al.* 2014; Battistoni *et al.* 2015) which can estimate the radioactive nuclides produced and the energy spectra of the post-PIC-generated particles. These estimations are useful in nuclear waste management (199 1998), positron annihilation lifetime spectroscopy (Audet *et al.* 2021), e^-–e^+ plasma studies (Chen *et al.* 2011; Sarri *et al.* 2015) and nuclear medicine (Schneider *et al.* 2002).

This paper starts with a description of our numerical solution for the laser field under the tight-focusing scheme as described in Jeong *et al.* (2015) (for LP lasers) and Jeong *et al.* (2018) (for RP and AP lasers). Based on the choice of a single-cycle pulse, the

https://doi.org/10.1017/S0022377821001318 Published online by Cambridge University Press

laser focuses in a sphere of diameter $\sim\lambda/2$ (λ^3 regime), for which an analytical estimation of the peak intensity is obtained. It is found that an ∼80 PW laser leads to a peak intensity of 10^{25} W cm^{-2}. The λ^3 regime exhibits a complex interaction with a foil target as discussed in § 3.1, regardless of the great simplicity of the problem compared with multi-cycle pulses interacting with sophisticated target geometries. Sections 3.2 and 3.3 describe the evolution of γ-photons and e^-–e^+ pair generation. Ballistic evolution of the γ-photons reveals a multi-PW γ-ray flash, expanding with preference to certain directions depending on the laser polarisation mode. A multi-parametric dependency of the laser energy transferred to each particle species is presented in § 3.4, where the variables include the target thickness, electron number density and laser polarisation. At the optimal combination of parameters, κ_γ is approaching 50 %, accompanied by a laser to positron energy conversion efficiency, κ_{e+}, of ∼10 %. Our results are generalised in § 3.5 for laser powers in the range 1 PW $\leqslant P \leqslant$ 300 PW, revealing a saturating trend for κ_γ, along with an optimum region of e^-–e^+ pair avalanche altering the γ-photon spectrum. As a final step, in § 4 the obtained γ-ray flash is combined with MC simulations in the vicinity of a high-Z secondary target, to elucidate the importance of the photonuclear interactions.

2. Simulation set-up

2.1. *Configuration of the λ^3 fields*

Since the paraxial approximation frequently used by default in PIC codes fails to correctly form the fields in the λ^3 regime, we followed a method where the electromagnetic fields are pre-calculated based on the tight-focusing scheme. We have obtained numerical solutions to the theory described in Jeong *et al.* (2015) for a LP tightly focused laser, where the validity of the model can be applied for $f_N \geqslant 1/4$. We have then extended our numerical solutions for a RP laser and an AP laser, based on the theoretical solutions in Jeong *et al.* (2018). Here, we describe the basic steps followed in order to calculate the λ^3 fields on focus, through a Fortran program we developed.

We assume a laser before parabola having a uniform spatial profile (a super-Gaussian profile of which the order goes to infinity) of diameter D, and that the beam is decomposed to the sum of fundamental wavelengths (Böhle *et al.* 2014), corresponding to a minimum wavelength of $\lambda_{\min} = 700$ nm, a maximum wavelength of $\lambda_{\max} = 1750$ nm, a central wavelength of $\lambda_c = 1000$ nm and equally spaced, equally weighted wavevector intervals (for mathematical simplification) of $\mathrm{d}k = (1/\lambda_{\min} - 1/\lambda_{\max})/(\lambda_{\max} - \lambda_{\min})$.

The integral over all wavevectors (with zero carrier envelope phase) gives the electric field of the plane wave laser (before parabola) as

$$E_{pw}(t) = \frac{\sin(2\pi ct/\lambda_{\max}) - \sin(2\pi ct/\lambda_{\min})}{t(2\pi c/\lambda_{\max} - 2\pi c/\lambda_{\min})}, \tag{2.1}$$

which, when squared, corresponds to the intensity as plotted by the red line in figure 1(*a*). The envelope of the laser is obtained by the Fourier transform of the flat-top spectral power range, resulting in an electric field envelope of

$$E_{sinc}(t) = \frac{\sin[\pi ct(1/\lambda_{\min} - 1/\lambda_{\max})]}{\pi ct(1/\lambda_{\min} - 1/\lambda_{\max})}, \tag{2.2}$$

while the corresponding intensity is shown by the blue dashed line in figure 1(*a*) and corresponds to a pulse duration of ∼3.4 fs at full width at half maximum (FWHM).

The calculation of electric and magnetic field components is performed in a Cartesian three-dimensional grid. Let E^2_{sum} be the sum of the squared electric field over all grid

https://doi.org/10.1017/S0022377821001318 Published online by Cambridge University Press

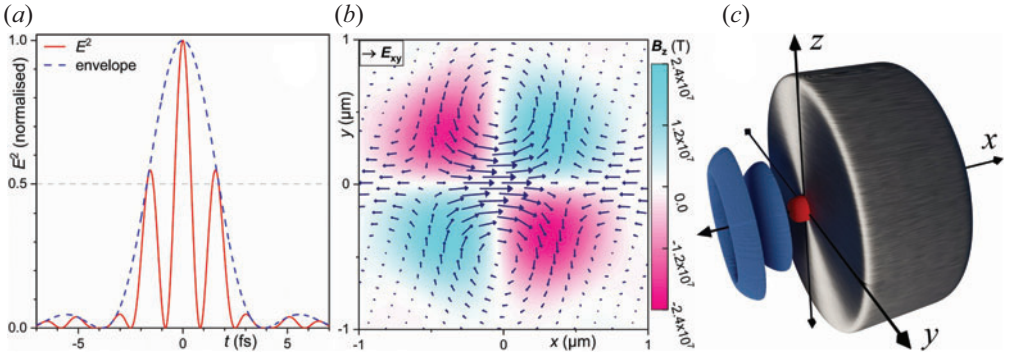

FIGURE 1. (*a*) The E^2 profile of the unfocused laser as a function of time is shown by the red line, as described in § 2.1. The blue dashed line shows the pulse envelope, with a pulse duration of ∼3.4 fs. (*b*) Electromagnetic field representation of the λ^3 laser, for the laser parameters used in this paper. The black arrows correspond to the electric field vectors, over-plotted on a contour of the magnetic field, on the *xy* plane. The result is obtained after free-propagating the externally calculated fields into EPOCH, near focal position (at approximately −0.3 fs). This field corresponds to a time-averaged peak intensity of 10^{25} W cm^{-2}. (*c*) Schematic representation of the simulation set-up. The grey cylinder represents the target. The blue intensity isosurface at 2×10^{24} W cm^{-2} corresponds to the externally imported electric and magnetic fields before propagation. The red intensity isosurface (FWHM of peak intensity) shows the λ^3 laser, corresponding to (*b*).

locations, for all three Cartesian components. By setting V as the volume of each computational cell, the laser energy corresponding to the electric field is

$$\mathcal{E}_E = \frac{\varepsilon_0 E_{\text{sum}}^2}{2} V. \tag{2.3}$$

The energy contribution of the magnetic field is equal to that of the electric field, resulting in a laser energy of $\mathcal{E}_l = \varepsilon_0 E_{\text{sum}}^2 V$. By knowing the total laser energy, one can weight accordingly each fundamental frequency contribution, with a weight coefficient W. In our specific case, $\mathcal{E}_l = 280$ J, resulting in a laser power of ∼80 PW.

The core part of our solution is the estimation of the three electric and three magnetic field components at each cell of a three-dimensional computational grid. To do so, at each cell we first sum the field contribution from the incident monochromatic electric field on the focusing optic surface over the azimuthal angle ($0 \leqslant \phi < \pi$) and the polar angle ($\theta_{\min} \leqslant \theta \leqslant \pi$, where $\theta_{\min}$ is given in Jeong *et al.* (2015) as a function of f and D) and then sum the contribution from each fundamental wavelength. Therefore, a six-fold Do-loop with Open Multi-Processing Application Programming Interface is employed, with the layer order from outer to inner being $y \to z \to x \to \lambda \to \theta \to \phi$.

Before solving the field integrals, we calculate a set of interrelated quantities independent of the grid position, $k = 2\pi/\lambda$, $A = \sin(\theta)/[1 - \cos(\theta)]$ and $B = [1 - \cos(\theta)]/(2kf)$. Three simplification variables connected to the grid location are also calculated, $X = \{2f\cos(\theta) - x[1 - \cos(\theta)]\}/(2f)$, $Y = \{2f\sin(\theta)\cos(\phi) - y[1 - \cos(\theta)]\}/(2f)$ and $Z = \{2f\sin(\theta)\cos(\phi) - z[1 - \cos(\theta)]\}/(2f)$. Then, a phase term is calculated, $F = k[x\cos(\theta) + y\sin(\theta)\cos(\phi) + z\sin(\theta)\sin(\phi)]$.

The above expressions simplify the integrands (integrated over θ and ϕ) from Jeong *et al.* (2015, 2018) into the form shown in Appendix A for a LP laser and in Appendix B for a RP laser. For an AP laser we interchange the integrands of the electric and magnetic

https://doi.org/10.1017/S0022377821001318 Published online by Cambridge University Press

terms. The electric field of a RP laser along the laser propagation direction is then

$$E_x = \frac{f}{\lambda_c} \sum_{\lambda=\lambda_{\min}}^{\lambda_{\max}} W \sum_{\phi=0}^{2\pi} \sum_{\theta=\theta_{\min}}^{\pi} I_{Ex-R} \tag{2.4}$$

(where I_{Ex-R} is given by (B1)), which is scaled by multiplying by $2\pi(\pi - \theta_{\min})/(n_\theta n_\phi)$, where n_θ and n_ϕ are the numbers of elements in the θ-array and ϕ-array, respectively. By calculating E_x, E_y, E_z in all grid locations, we obtain the three arrays containing the components of the electric field, whilst the same process is applied for the magnetic field calculation.

2.2. *Laser intensity in the λ^3 regime*

In order to find an approximate value of the peak laser intensity, I_p, we consider only the central peak of the electric field, as shown in figure 1(*a*) for -0.8 fs $\lessapprox t \lessapprox 0.8$ fs, containing $\sim(1/3)\mathcal{E}_l$ at FWHM (temporal profile). In addition, we consider that an Airy function (Born & Wolf 1964) (formed due to focusing of the laser) corresponds to $\sim(1/2)\mathcal{E}_l$ at FWHM (spatial profile). In the λ^3 regime, the laser field corresponds to a spherical volume, V_S, of diameter $\sim\lambda/2$. The focused fields are obtained by setting $f_N = 1/3$ in § 2.1. By combining the above, and transforming the temporal dimension in space, we get

$$I_p = \frac{c\mathcal{E}_l/6}{V_S} = \frac{8c\mathcal{E}_l}{\pi\lambda^3}. \tag{2.5}$$

In this work $\mathcal{E}_l = 280$ J (apart from § 3.5) and $\lambda = 1$ μm, where (2.5) gives $I_p \approx 2 \times 10^{25}$ W cm^{-2}, or a most commonly used time-average intensity (or simply intensity) of $I \approx 10^{25}$ W cm^{-2}.

The peak intensity can also be calculated in the basis of a more strict definition. The spatial boundary of the λ^3 regime corresponds to the first minima of the Airy function, which requires reduction to $\sim$83.8 % of $\mathcal{E}_l$. On the temporal dimension, consideration of only the central peak of the electric field (as previously) requires further reduction to $\sim$44.2 % of $\mathcal{E}_l$, reducing it to $\mathcal{E}_l \to 0.838 \times 0.442 \times 280$ J ≈ 104 J.

The energy fraction contained in the sphere of Gaussian profile in all directions and of radius r and standard deviation $\sigma = \sqrt{8\ln(2)}$ FWHM can be calculated as

$$\int_0^{2\pi}\int_0^{\pi}\int_0^{r} \left(\sigma\sqrt{2\pi}\right)^{-3} \exp\left[-\frac{1}{2}\left(\frac{r}{\sigma}\right)^2\right] r^2 \sin(\theta)\, \mathrm{d}r\, \mathrm{d}\theta\, \mathrm{d}\phi$$
$$= \operatorname{erf}\left(\frac{r}{\sqrt{2}\sigma}\right) - \sqrt{\frac{2}{\pi}}\frac{r}{\sigma}\exp\left[-\frac{1}{2}\left(\frac{r}{\sigma}\right)^2\right]. \tag{2.6}$$

Dividing (2.6) by the volume of the sphere, taking the limit as $r \to 0$, and using l'Hospital's rule once, we estimate

$$\lim_{r\to 0} \frac{\operatorname{erf}\left(\frac{r}{\sqrt{2}\sigma}\right) - \sqrt{\frac{2}{\pi}}\frac{r}{\sigma}\exp\left[-\frac{1}{2}\left(\frac{r}{\sigma}\right)^2\right]}{\frac{4}{3}\pi r^3} = \frac{1}{(2\pi\sigma^2)^{3/2}}. \tag{2.7}$$

By considering the energy contained in the sphere, and transforming the spatial dimension in time, we obtain

$$I_p = \frac{c(0.838 \times 0.442 \times \mathcal{E}_l)}{(2\pi\sigma^2)^{3/2}}. \tag{2.8}$$

https://doi.org/10.1017/S0022377821001318 Published online by Cambridge University Press

By replacing $\sigma \approx \lambda/[4\sqrt{2\ln(2)}]$, (2.8) gives

$$I_p = \left[\sqrt{\frac{\ln(2)}{\pi}}\frac{4}{\lambda}\right]^3 c(0.838 \times 0.442 \times \mathcal{E}_l) \approx \frac{2.457 c\mathcal{E}_l}{\lambda^3}, \tag{2.9}$$

which again gives $I \approx 10^{25}$ W cm^{-2}.

By relating the intensity to the corresponding electric field through $E = \sqrt{2I/(c\varepsilon_0)}$, the focused laser gives $E \approx 8.7 \times 10^{15}$ V m^{-1}. This field gives a value for the dimensionless amplitude of $a_0 \approx 2700$, where in the laser interaction with a plasma, an electron typically gains a relativistic factor of $\sim a_0$.

2.3. *The PIC simulation set-up*

The results presented in this paper are obtained through three-dimensional PIC simulations by use of the EPOCH (Arber *et al.* 2015) code. The code is compiled with the flags for quantum electrodynamics (Ridgers *et al.* 2014) and Higuera–Cary (Higuera & Cary 2017) preprocessor directives enabled. The quantum electrodynamics module enables γ-photon and e^-–e^+ pair generation, the inclusion of which is essential at ultra-high intensities. Since γ-photon generation is directly connected with electron/positron energy and trajectory, an accurate estimation of their motion is necessary. The Higuera–Cary solver accounts for the necessity of increased motion accuracy, since the default Boris solver (Boris 1970) is less reliable for relativistic particles. Both ionisation and collisional processes are neglected in our PIC simulations; the energy contained in the laser pulse is six orders of magnitude larger than that needed to fully ionise a titanium sphere of radius $\lambda/2$.

No laser block is used in our simulations. Instead, we take advantage of the EPOCH fields block, which enables the import of a desired electromagnetic field configuration as three electric and three magnetic field components. The field data were pre-calculated (as described in § 2.1) in a three-dimensional grid matching the number of cells per dimension with those used in the PIC grid. The fields have a zero carrier envelope phase, as this is found to benefit κ_γ in the λ^3 regime. In this work we define that the laser is focused at $t = 0$ fs, as shown in figure 1(*b*). The imported unfocused field data were calculated at $t \approx -4.27$ fs. The simulation set-up is shown in figure 1(*c*), where the imported fields are overlapped with the target geometry.

The three-dimensional EPOCH grid is cubic, with the focal spot defined at the centre of the cube. All three dimensions extend from -5.12 to 5.12 μm with 1024 cells per dimension. The resulting cells are cubes with an edge of $\alpha_c = 10$ nm. The highest electron number density used is 5×10^{24} cm^{-3}, for which, at an intensity of 10^{25} W cm^{-2}, the relativistically corrected skin depth is resolved with an accuracy of more than 10 cells per skin depth. At that electron number density, the skin depth can be resolved even with intensities as low as 10^{21} W cm^{-2}. The simulation stops after 16 fs, since beyond that time fields start escaping the simulation box, for which we have set open boundary conditions. The box dimensions are chosen large enough that the laser to each particle species energy conversion efficiency, κ, saturates.

The particle species set at code initialisation are ions and electrons, while γ-photons and e^-–e^+ pairs are generated during code execution. The ion atomic number is set to $Z = 1$, while its mass number is $A = 2.2$, which is the average A/Z for solid elements with $Z < 50$. EPOCH behaviour was tested by multiplying Z and A by a factor and simultaneously reducing the ion number density by the same factor, giving identical results. Therefore, our

https://doi.org/10.1017/S0022377821001318 Published online by Cambridge University Press

	e^- ($\mathcal{E}_e < 500$ MeV)	e^- ($\mathcal{E}_e > 500$ MeV)	γ-photon ($\mathcal{E}_\gamma > 500$ MeV)
RP laser	99 MeV	204 MeV	139 MeV
LP laser	128 MeV	172 MeV	178 MeV
AP laser	96 MeV	280 MeV	147 MeV

TABLE 1. The temperature of electrons and γ-photons for RP, LP and AP lasers.

simulations can be generalised for most target materials used in laser–matter interaction experiments.

The target geometry is cylindrical, with the cylinder radius being $r = 2.4$ μm and the height of the cylinder (target thickness), l, varying in the range $0.2\ \mu\text{m} \leqslant l \leqslant 2\ \mu\text{m}$. Although the target can be considered as mass-limited, its radius is large enough that its periphery survives the laser–foil interaction by the end of the simulation. The target front surface is placed at $x = 0$ μm, coinciding with the focal spot. The electron number density is uniform for each simulation, and is within the range $2 \times 10^{23}\ \text{cm}^{-3} \leqslant n_e \leqslant 5 \times 10^{24}\ \text{cm}^{-3}$. In order to have eight macroparticles per cell (eight macroions and eight macroelectrons), the number of ions and initial electrons is set to $8\pi r^2 l/\alpha_c$. Since spectral extrapolation reveals that γ-photons with energy <1 MeV account for $\sim 1\,\%$ of the γ-photon energy, only those above that energy threshold were allowed in the simulation.

3. Results and discussion

The present section provides a detailed description on the interaction of the ultra-intense laser with a solid target in the λ^3 regime, for RP, LP and AP lasers. In §§ 3.1, 3.2 and 3.3 the description is made for a relatively thick target (2 μm) with an electron number density similar to that of titanium ($1.2 \times 10^{24}\ \text{cm}^{-3}$).

3.1. *Electron evolution*

A schematic representation of the simulation set-up used in the current subsection is shown in figure 1(*c*), where a λ^3 pulse interacts with a 2 μm thick cylindrical target of electron number density of $1.2 \times 10^{24}\ \text{cm}^{-3}$. These target parameters correspond to the highest κ_γ achieved in our simulations for an ∼80 PW laser, approaching 50 %. The interaction results in a double exponentially decaying electron spectrum for all three polarisations, where the first exponential is in the energy range of approximately $200\ \text{MeV} \leqslant \mathcal{E}_e \leqslant 500$ MeV and the second is $\gtrsim$500 MeV. The temperature of the lower-energy part of the spectrum is ∼100 MeV and approximately double for the higher-energy part. These electrons are accompanied by an ion spectrum of similar temperature, a Maxwell–Juttner-like positron spectrum and a γ-photon exponentially decaying spectrum of temperature ∼150 MeV. The exact temperatures for electron and γ-photon spectra for RP, LP and AP lasers are summarised in table 1.

As mentioned earlier in § 1, one fundamental difference of a RP laser and an AP laser (tightly focused) is the presence and the absence of E_x, respectively (Jeong *et al.* 2018). For a LP laser of the same power, although resulting in higher intensity, E_x is weaker than that of the RP laser. For a tightly focused laser, E_x dominates over E_r, as seen from the centre of figure 1(*b*). Another field feature for the tight-focusing scheme is the curled field vectors centred at a distance of $\sim\lambda/2$ from focus. This pattern can be understood as an interference of the Airy pattern for a plane wave, when tightly focused. For the AP laser,

https://doi.org/10.1017/S0022377821001318 Published online by Cambridge University Press

the electric and magnetic field roles are interchanged, where the electric field now has a rotating form around the laser propagation axis.

Figure 1(*b*) reveals the complexity of the λ^3 laser due to interplay of all three field components, versus two for weak focusing. Furthermore, the single-cycle condition breaks the repetitive nature of a multi-cycle laser, where despite limiting the laser–foil interaction in the wavelength time scale, each time has a unique effect on the evolution of the interaction. That complicated field behaviour results in a significantly different laser–foil interaction, depending on the laser polarisation. For RP, LP and AP lasers, κ is significantly different, since the electron trajectories are completely incomparable.

Let us consider the case of a RP laser. As a result of the laser–foil interaction a conical-like channel is progressively drilled on the foil target by the laser field, where the ejected electrons are either rearranged in the form of a low-density pre-plasma distribution or reshaped as thin over-dense electron fronts. The conical channel formation is mainly mandated by E_x, although its formation initiates by the pulse edges even prior to the arrival of the focused pulse. The dimensions of the channel are in agreement with the pulse extent, of $\sim\lambda/2$.

The channel formation is considered in three time intervals of $t_a < -\lambda/(4c)$, $-\lambda/(4c) \leqslant t_b \leqslant \lambda/(4c)$ and $t_c > \lambda/(4c)$. At t_a, although the peak laser field has not yet reached the focal spot, a low-amplitude electric field exists due to the sinc temporal profile (see figure 1*a*). Those pulses, although several orders of magnitude lower than the peak laser field, are still capable of heating and driving electrons out of the target. In addition, the field corresponding to the outer Airy disks of the main pulse is also capable of affecting the target electrons. Their combined effect is deformation of the steep flat target density profile. At -1.3 fs, the target profile consists of a submicrometric under-dense region at the target front surface, followed by an over-dense tens-of-nanometres-thick electron pileup and then by the rest of the intact target. At that stage a directional ring of high-energy electrons also appears at $\sim 60^\circ$ to the target normal, connected with the focusing conditions ($f_N = 1/3$) of the laser field. Finally, a high-energy electron population is moving along the laser propagation axis. The momentum of all electron groups is governed by a characteristic time interval of $\lambda/(4c)$.

The upper row of figure 2 shows the polar energy spectrum of electrons for three polarisations at 0.7 fs. At t_b, the curled part of the electric field changes the directionality and distribution of the thin electron ring population, transforming it into a toroidal-like electron distribution with a torus radius of $\sim\lambda/2$, matching the centre of the curled field. Simultaneously, the peak E_x reaches the focal spot without any significant decay, since the toroidal-like electron distribution allows for a practically vacuum region for the field to propagate. At -0.3 fs the electron energy distribution reaches energies of ~ 1 GeV. However, after a time of $\lambda/(4c)$ the pulse is reflected by the thin over-dense electron front. By the time the pulse is reflected, the electron population corresponding to the toroidal structure emerges into a closed high-energy electron distribution, which can be considered as a pre-plasma at the target front surface.

Within t_b, high-amplitude oscillations of the electron momentum occur. At t_c, electron momentum oscillations become gradually less significant, with the electron spectrum eventually saturating. At this stage, the peak laser field is not completely reflected, but E_x starts forming a cavity beyond the over-dense electron front. Part of the laser field then reaches within the cavity, further expanding it. The initial times of this process witness instantaneous intensities an order of magnitude higher than the intensity expected on focus, due to interference of the laser fields after diffraction/reflection by the cavity walls. Although the intensity occurs only instantaneously, it was found to be $\sim 8.8 \times 10^{25}$ W cm^{-2} in a region approximated by a sphere of ~ 50 nm diameter, at 1.7 fs.

https://doi.org/10.1017/S0022377821001318 Published online by Cambridge University Press

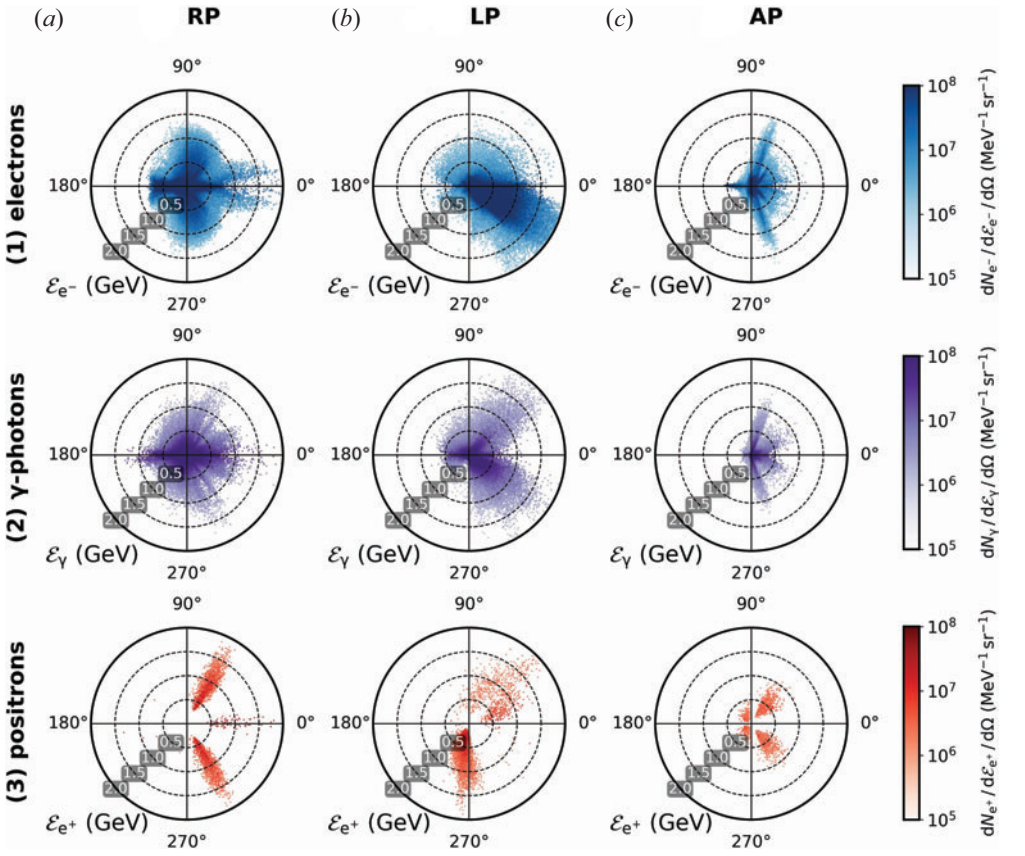

FIGURE 2. Polar energy spectrum diagrams of (1) electrons at ∼0.7 fs and (2) γ-photons and (3) positrons generated in the time interval -0.3 fs $\leqslant t \leqslant 0.7$ fs, for (*a*) a RP laser, (*b*) a LP laser and (*c*) an AP laser. Animation for a larger time interval is provided in supplementary movie 1.

At this stage, another electron population emerges, driven by the reflected field in the backward direction. In summary, during all stages of the laser–target interaction, electron populations at 0°, ∼60° and 180° are recorded.

So far, we have given a detailed explanation of the electron evolution under the influence of a RP λ^3 laser. For a LP λ^3 laser, although the E_x still does exist, the lack of rotational symmetry does not allow the curled fields to take a toroidal form. Therefore, although a pre-plasma distribution is formed, it is extremely asymmetric along the laser oscillation direction. The thin over-dense electron pileup is also asymmetric. The asymmetry is due to the initial decay of the flat target, diverting the laser into a favourable direction. Asymmetric field interference does not allow the laser to form a conical cavity, but the random nature of the process forms a macroscopically rectangle-like cavity instead.

For the case of an AP λ^3 laser the cavity formation is simpler. The absence of E_x means that the laser can be absorbed by the target in a manner similar to that of a weakly focused laser, suppressing the target deformation. The deformation takes the form of an over-dense electron pileup without pre-plasma. The pre-plasma created is also suppressed, in a region near the laser propagation axis. However, by the end of the simulation a cavity is eventually created, although by that time strong fields do not exist and κ_γ is limited, as discussed in § 3.2.

https://doi.org/10.1017/S0022377821001318 Published online by Cambridge University Press

3.2. *Evolution of γ-photons and positrons*

At ultra-high laser intensities, γ-photon and e^-–e^+ pair generation plays an important role in the laser–target interaction. The non-trivial form of the λ^3 field reveals a strong dependency of γ-photon and e^-–e^+ pair generation every quarter-period, in connection with the altered gradient/sign of the laser field, which in extension defines the electron motion as seen in § 3.1.

The γ-photon generation can be visualised by a series of polar energy spectrum diagrams. An animation for various times is provided as supplementary material movie 1 available at https://doi.org/10.1017/S0022377821001318. However, since we are mainly interested in the evolution of γ-photon generation, it is more appropriate to consider the difference of every two subsequent polar diagrams, where our simulations output the data every 1 fs, a time interval similar to the quarter-period of 5/6 fs. The second row of figure 2 (see also the second row in supplementary movie 1) shows these diagrams for the three polarisations used, for a time interval of $-0.3\ \text{fs} \leqslant t \leqslant 0.7\ \text{fs}$. These diagrams have the benefit of not only showing at which angle γ-photons are generated, but also a negative value indicates γ-photon loss. In our simulations no γ-photons are allowed to escape the simulation and lack of γ-photons is attributed only to e^-–e^+ pair formation. The corresponding plots for positrons are shown in the third row of figure 2. We must clarify that γ-photons and e^-–e^+ pairs are not only formed in positive and negative polar diagram values, respectively, but a negative sign means that more γ-photons are lost to e^-–e^+ pairs than are generated by the multi-photon Compton scattering process.

Let us consider a RP laser. Initially, up to -2.3 fs, only a small fraction of electrons obtain relativistic energies due to the low-amplitude periphery of the λ^3 field. These electrons then interact with the reflected relatively low-amplitude edge of the laser (Ridgers *et al.* 2012) producing low-energy ($\sim$0.1 GeV) γ-photons. However, during the next femtosecond significantly more electrons acquire relativistic energies and in combination with the increased amplitude of the field as approaching the focal spot at $\sim 60^\circ$, directional γ-photons of $\sim$0.5 GeV appear at the same angle. In addition, another energetic electron population appears towards the laser propagation axis, producing another high-energy γ-photon population.

A similar process continues up to -0.3 fs, although electric fields are intensified giving γ-photons of $\sim$1 GeV. The newly generated γ-photons are still oriented purely at a $\sim 60^\circ$ cone and also on the laser axis. It is no surprise that the γ-photon yield continues increasing until the laser pulse peak amplitude reaches the focal spot. What is a surprise is that the high-energy part of the γ-photon spectrum drops near that time. The overall increase in κ_γ is mostly due to an isotropic generation of moderate- to low-energyγ-photons.

In figure 2(*c*), one can observe the polar energy spectrum of positrons generated within 1 fs time interval at $\sim 60^\circ$, corresponding to the conversion of high-energy γ-photons to e^-–e^+ pairs. Strong e^-–e^+ pair generation continues within the next 2 fs and then sharply decreases. This time interval is characterised by a region of negative values (γ-photon loss) in the high-energy part of the γ-photon energy spectra produced within a finite time, when plotted as a function of time. This plot (not shown) reveals the quarter-period behaviour of γ-photon generation as a superposition of several peaks. As the field amplitude drops, the γ-photon production rate also drops. One can approximate the γ-photon production rate as a steep Gaussian-like function up to the focus, followed by an exponential-like decay.

As mentioned in § 1, a LP laser results in a higher peak intensity compared to a RP laser of the same power. Although the lack of symmetry results in a weaker coupling of the laser

https://doi.org/10.1017/S0022377821001318 Published online by Cambridge University Press

energy to the target electrons, the higher intensity on focus results in a slight enhancement of the high-energy part of the γ-photon energy spectrum for the LP laser case. However, at energies lower than $\sim$0.37 GeV the amplitude of the γ-photon energy spectrum is higher for the RP laser case. Consider that for the RP laser, γ-photons with energy $<\sim$0.37 GeV contain $\sim$90 % of the γ-photon energy. Therefore, although the LP laser results in higher cut-off energies, it results in κ_γ of $\sim$40 %, compared with $\sim$47 % for a RP laser. For the AP laser, although strong fields do exist, the Lorentz factor of electrons is significantly lower than for the other two polarisation cases. Furthermore, no significant pre-plasma is formed in the laser field reflection region. As a result, κ_γ of only $\sim$20 % occurs.

The positron spectra for LP and RP lasers overlap, apart from in the very high and very low parts of the spectra, where the positrons obtain κ_{e+} $\sim$7 % and $\sim$9 %by the end of the simulation. However, this energy is not purely a result of γ-photon energy conversion to e^-–e^+ pairs, but it is also a result of acceleration/deceleration of those positrons by the laser field, in the same manner as electrons (Ridgers *et al.* 2012). One index that can directly compare two interactions is the number of positrons generated, regardless of their energy, where for a RP laser and a LP laser we obtain $\sim 5.7 \times 10^{11}$ and $\sim 4 \times 10^{11}$ positrons, respectively. In comparison, the AP laser results in κ_{e+} $\sim$3 %, but generation of only $\sim 1.9 \times 10^{11}$ positrons. The imbalance of κ_{e+} to number of positrons for the various laser polarisation modes verifies that positrons are strongly affected by the laser field after their generation.

In addition, our simulations record local positron number densities as high as $\sim 3 \times 10^{26}$ cm^{-3}, approximately two orders of magnitude higher than the titanium target electron number density, emphasising the collective effect of e^-–e^+ pairs in the laser–targetinteraction. By assuming that the e^-–e^+ pairs are contained in a uniform density sphere of diameter equal to that of the λ^3 laser, they correspond to an average number density of $\sim 10^{25}$ cm^{-3}, still an order of magnitude higher than the target electron number density.

3.3. *The γ-ray flash*

As mentioned in Hadjisolomou *et al.* (2021), the γ-photons generated during the interaction of a RP λ^3 laser with a foil appear in the form of a spherically expanding shell. The γ-photon energy density of this shell is not uniform since more energetic γ-photons are at 0°, 180° and $\sim$60°. Computational constraints limit the γ-photon shell expansion within a cube of $\pm$5.12 μm edges. In the EPOCH code, if a γ-photon is not lost to an e^-–e^+ pair, then it propagates ballistically. Therefore, the γ-photon located at position $(x_{i,1}, y_{i,1}, z_{i,1})$ can propagate a distance $\mathcal{D}$ to a new position $(x_{i,2}, y_{i,2}, z_{i,2})$ (where the subscript i denotes the corresponding γ-photon of energy $\mathcal{E}_i$):

$$x_{i,2} = x_{i,1} + \mathcal{D}p_{i,x}/\sqrt{p_{i,x}^2 + p_{i,y}^2 + p_{i,z}^2}, \tag{3.1}$$

$$y_{i,2} = y_{i,1} + \mathcal{D}p_{i,y}/\sqrt{p_{i,x}^2 + p_{i,y}^2 + p_{i,z}^2}, \tag{3.2}$$

$$z_{i,2} = z_{i,1} + \mathcal{D}p_{i,z}/\sqrt{p_{i,x}^2 + p_{i,y}^2 + p_{i,z}^2}, \tag{3.3}$$

which corresponds to a new distance r_i from the axis origin.

The ballistic γ-photon expansion for a $\mathcal{D}$ of 15.36 μm reveals that the γ-photon population at 60° rapidly decreases geometrically. However, the γ-photon populations at 0° and 180° due to their small solid angle are preserved, as shown in figure 3(*a*). The spherically expanding γ-ray flash at large distances is considered as originating

https://doi.org/10.1017/S0022377821001318 Published online by Cambridge University Press

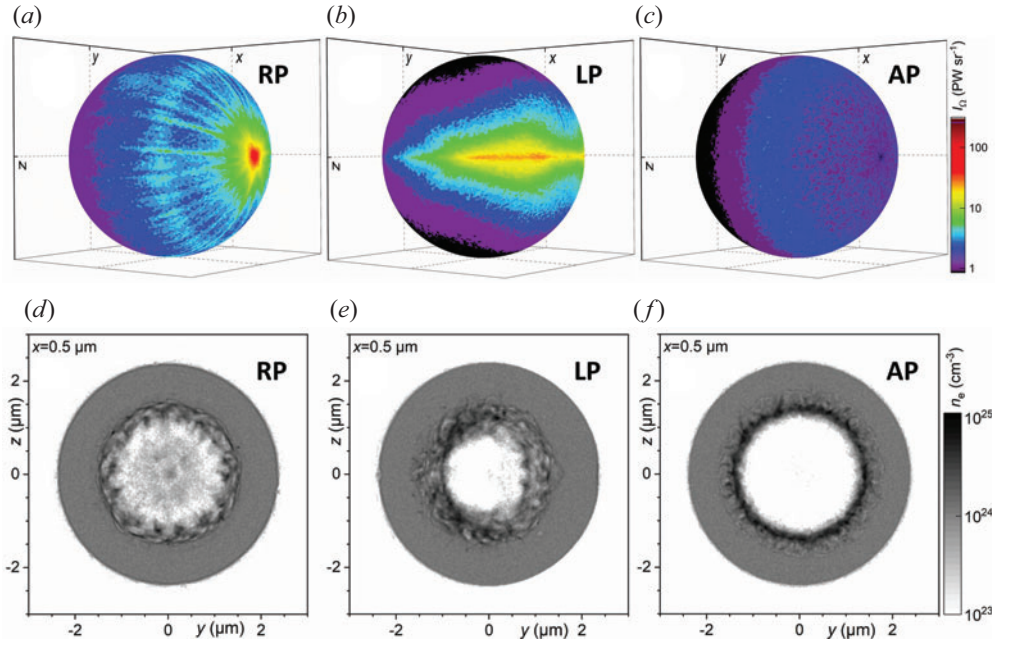

FIGURE 3. The γ-photon radiant intensity for (*a*) a RP laser, (*b*) a LP laser and (*c*) an AP laser, 64 fs after the start of the simulation. Electron number density cross-section at $x = 0.5$ μm for (*d*) a RP laser, (*e*) a LP laser and (*f*) an AP laser, at the end of the simulation.

from a virtual point source, although as seen in § 3.2 the γ-photons are not generated instantaneously.

As mentioned earlier for a RP laser, γ-photons obtain ∼47 % of the ∼280 J laser energy, or in other words, the γ-ray flash energy is ∼130 J. To calculate the mean location of the γ-ray flash, μ, we calculate the first-order moment as

$$\mu = \frac{\sum_i \mathcal{E}_i r_i}{\sum_i \mathcal{E}_i}, \tag{3.4}$$

which for the RP laser case gives $\mu \sim 18.5$ μm.

The second-order moment gives the position variance, σ^2, of the γ-ray flash as

$$\sigma^2 = \frac{\sum_i \mathcal{E}_i (r_i - \mu)^2}{\sum_i \mathcal{E}_i}, \tag{3.5}$$

while the square root of the variance gives the standard deviation, which in turn gives the temporal FWHM of the γ-ray flash. For a RP laser the γ-ray flash has a FWHM duration of ∼4.2 fs resulting in a γ-ray flash of ∼31 PW.

For a LP laser and an AP laser the γ-ray flash power is ∼28 and ∼13 PW, respectively. The AP laser results in high-energy γ-photons emitted mainly at ∼60°, while the dominant low-energy γ-photons are emitted isotropically, as shown in figure 3(*c*). The LP laser case results in two detached γ-photon fronts delayed by a half-period at $\sim \pm 45°$ and with higher γ-photon energy density on the plane defined by the laser field oscillation. At large

https://doi.org/10.1017/S0022377821001318 Published online by Cambridge University Press

	$\mathcal{E}_\gamma$ (J)	μ (μm)	σ (μm)	t_{FWHM} (fs)	P (PW)
RP laser	131	18.6	0.53	4.2	31
LP laser	113	18.6	0.52	4.1	28
AP laser	58	18.4	0.58	4.5	13

TABLE 2. Energy, mean position, position variance, duration and power of the γ-ray flash for RP, LP and AP lasers.

distances, these fronts merge, and therefore expand as thin rings, as seen in figure 3(*b*). The energy, mean position, position variance, duration and power of the γ-ray flash for RP, LP and AP lasers are summarised in table 2.

The electron number density for the RP laser case forms radially symmetric regular modulations inside the target cavity (figure 3*d*). The effect of those modulations is reflected in the γ-photon radiant intensity distribution, as shown in figure 3(*a*). For the LP laser case, although electron modulations are formed, they are symmetric only with respect to the laser oscillation direction (figure 3*e*). Therefore, radial γ-photon modulations are not observed (figure 3*b*) and any γ-photon modulation is hidden by the macroscopic γ-photon distribution. Similar patterns have been observed for a LP laser in both two-dimensional (Nakamura *et al.* 2012) and three-dimensional (Stark, Toncian & Arefiev 2016; Wang *et al.* 2020*a*) simulations. For the AP laser case, radial electron modulations are formed, but with outwards directionality. Furthermore, they are shielded inthe field region by an over-dense electron ring distribution (figure 3*f*). As a result, no obvious γ-photon modulations are observed.

3.4. *Mapping the energy conversion efficiency*

In the current subsection we present the results of our multi-parametric study for an ∼80 PW laser (RP, LP and AP laser cases) with κ_γ, κ_{e+}, laser to electron energy conversion efficiency κ_{e-} and laser to ion energy conversion efficiency κ_{i+}. The variable parameters include the target thickness and electron number density, for which the inversely proportional relation is mentioned in § 1. The results are presented in the form of ternary plots (West 1982) accompanied by radar charts.

Unavoidably, interaction of a laser field with matter results in transformation of some laser energy to particle energy. The dependency of κ on the electron number density and target thickness can be seen in figure 4, where the direction of the grey arrow in the figure indicates increasing thickness. For both RP and LP lasers, increased laser to all particles energy conversion efficiency, $\kappa_{\text{tot}} = \kappa_\gamma + \kappa_{e+} + \kappa_{e-} + \kappa_{i+}$, occurs for thicker and denser targets, ∼80 % and ∼85 % for RP and LP lasers, respectively. For thinner and low-density targets, the particles obtain only ∼40 % of the laser energy for both RP and LP lasers (within the parameter ranges examined). For an AP laser for thin and low-density targets, κ_{tot} is approximately half compared to that for RP and LP lasers. For an AP laser (in contrast to the continuously increasing κ_{tot} behaviour for RP and LP lasers) beyond of an optimal thickness–density combination, κ_{tot} starts decreasing for thicker and denser targets (maximum is ∼60 %), in connection with the inefficient target cavity formation (see § 3.1) and increasing laser back-reflection as electron number density increases.

In general, ions, being heavier than electrons, do not produce high-energy γ-photons. However, they indirectly affect the γ-photon spectrum. Their contribution arises from the amount of the laser energy transferred to them, consequently reducing electron energy

https://doi.org/10.1017/S0022377821001318 Published online by Cambridge University Press

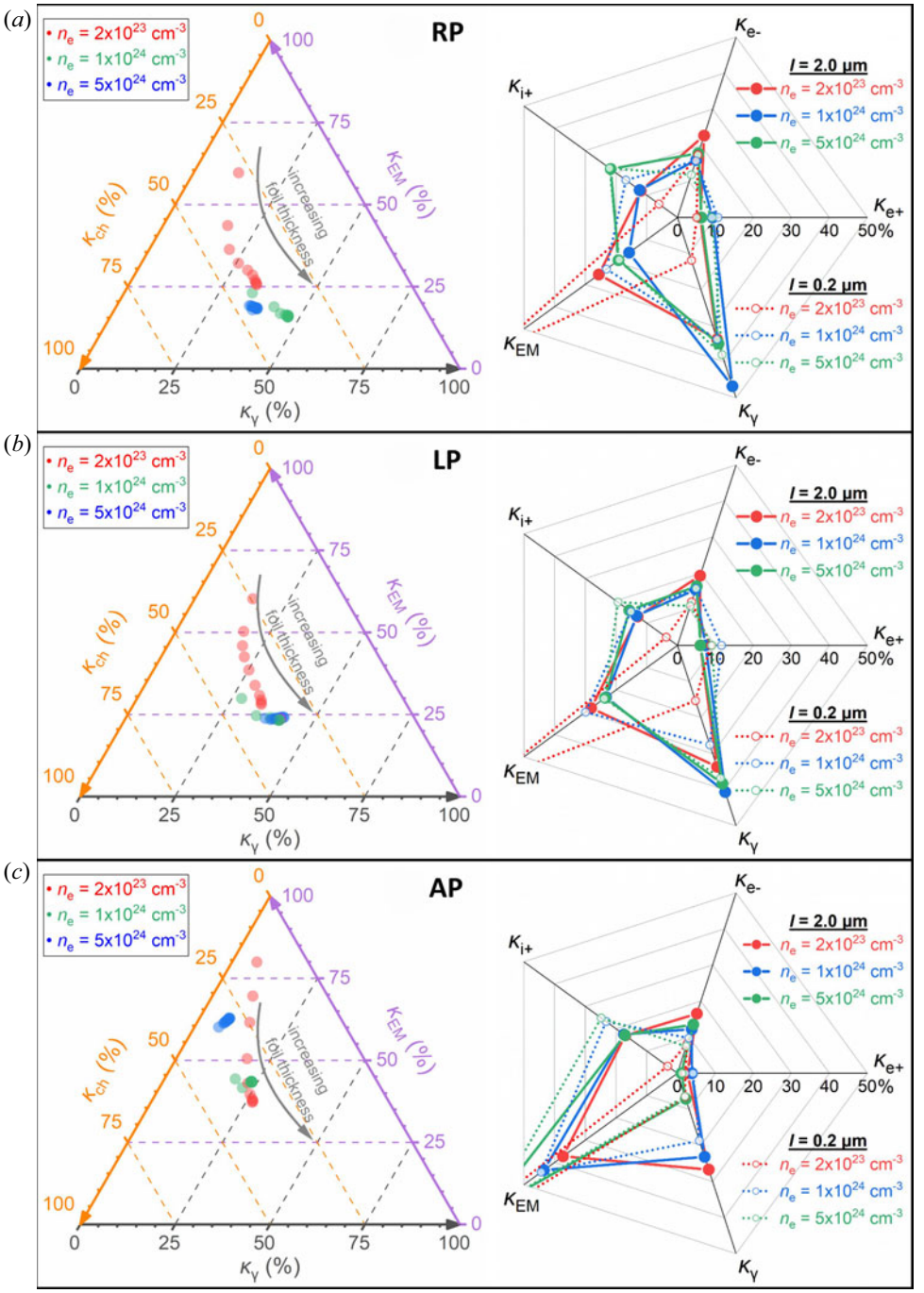

FIGURE 4. (Left) Ternary plots of κ_γ, κ_{ch} and κ_{EM} for samples with varying electron number density and target thickness. The grey arrow points towards increasing foil thickness. (Right) Selected radar charts (solid line for 2 μm and dotted line for 0.2 μm thick foil; red for 2×10^{23} cm^{-3}, blue for 1×10^{24} cm^{-3} and green for 5×10^{24} cm^{-3} electron number density) of κ_γ, κ_{e+}, κ_{e-}, κ_{i+} and κ_{EM}. (*a*) A RP laser, (*b*) a LP laser and (*c*) an AP laser.

https://doi.org/10.1017/S0022377821001318 Published online by Cambridge University Press

and therefore what can otherwise be converted to γ-photons. For all polarisation cases, κ_{i+} increases with increasing electron number density up to an optimum value and then decreases for thicker targets (Esirkepov *et al.* 2004; Klimo *et al.* 2008; Robinson *et al.* 2008; Bulanov *et al.* 2016). Therefore, although thin targets can be dense enough to convert a large fraction of laser energy to particle energy, that energy goes primarily to ions. For thick targets, although more laser energy is converted to particle energy by increasing the electron number density, since κ_{i+} also increases, it competes with what is converted to κ_γ, κ_{e-} and κ_{e+}, forbidding the optimum of those particles to exist at extremely high electron number density values. For optimal thickness and density combinations, for all three polarisations, κ_{i+} reaches $\sim$25 %.

Where κ_{i+} is not efficient, κ_{e-} and κ_{e+} cover the imbalance. For all laser polarisation modes, if the electron number density is extremely low then the laser pulse propagates through the target. Alternatively, if the target is thick enough then most of the laser energy is absorbed, resulting in enhanced κ_{e-}. For RP and LP lasers, κ_{e-} is $\sim$20 %, while for an AP laser it is $\sim$15 % at optimum target parameters. Some slow κ_{e-} increase for extremely high electron number densities is due to less accurate resolution of the relativistically corrected skin depth, although the increase is insignificantly small to alter the conclusion of the other particle species at that density. For RP and LP lasers, a high κ_{e-} also occurs for thin targets in regions where κ_{i+} is not efficient, due to electron capture by the laser field (Wang *et al.* 2001).

Although for an $\sim$80 PW laser a significant number of e^-–e^+ pairs are generated, their number is still relatively low (approximately 50 times lower) compared with the number of electrons contained in the target prior to the laser–foil interaction. However, those e^-–e^+ pairs are generated in regions of ultra-intense fields, and therefore are more strongly heated compared with the electrons in the periphery of the target cavity. The e^-–e^+ pairs more probably originate from γ-photons of higher energy. Therefore, κ_{e+} is a combination of the energy they obtain from the Breit–Wheeler process and the energy due to acceleration/deceleration from the laser field. The thickness–density contour of κ_{e+} has partial topological similarities to that of κ_{i+}, meaning that positrons are affected by the laser field in a manner similar to that of ions. The κ_{e+} for RP and LP lasers reaches $\sim$10 %, while it is approximately half for an AP laser. In contrast to electrons, positrons cannot obtain high κ_{e+} for under-dense thick targets because of their low number generated at these parameter values.

By combining the laser to all charged particles energy conversion efficiency, $\kappa_{ch} = \kappa_{e+} + \kappa_{e-} + \kappa_{i+}$, we conclude a maximum value of $\sim$45 % that slowly increases with increasing target thickness, as shown in figure 4. On the other hand, the figure exhibits a steep increase of κ_γ for increasing target thickness, where the maximum values are mentioned in § 3.2. For a LP laser, the topology of the κ_γ thickness–density contour is in agreement with that of κ_{tot}, being maximised for thick and dense targets. On the other hand, for the RP laser, although the κ_γ thickness–density contour resembles that of the LP laser for most thickness–density combinations, a maximum is observed at an electron number density of 1.2×10^{24} cm^{-3}. This local maximum is due to the different rate of energy transfer to ions, where for a RP laser it is lower at that electron number density. In addition, κ_{tot} is slightly higher for the RP laser at thicker and denser targets, further enhancing the local maxima of κ_γ. For an AP laser, κ_γ has an optimal electron number density at 5×10^{23} cm^{-3} since the lack of E_x requires a target of lower electron number density for efficient laser–target coupling. For more accurate κ for each particle species at the extreme thickness–density values, see the right-hand side of figure 4.

https://doi.org/10.1017/S0022377821001318 Published online by Cambridge University Press

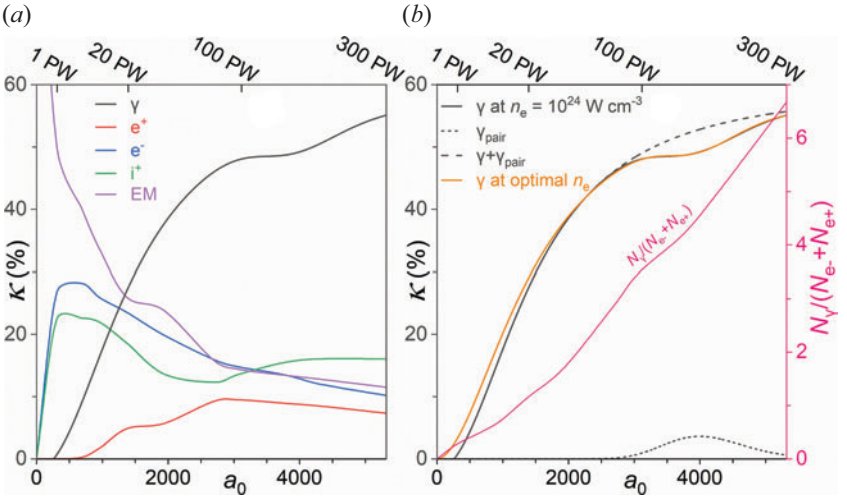

FIGURE 5. Values of (*a*) κ_γ (black line), κ_{e+} (red line), κ_{e-} (blue line), κ_{i+} (green line) and κ_{EM} (purple line) as a function of a_0 for a RP λ^3 laser and an electron number density of 10^{23}–10^{24} cm^{-3}. (*b*, left-hand axis) Plot of κ_γ fitted with (3.6) for an electron number density of 10^{23}–10^{24} cm^{-3} (black solid line) and at the optimum electron number density at each power (orange line). The fitted curve is the difference of a 'Logistic' function (long-dashed black line) and a 'LogNormal' function (short-dashed black line), as defined in the text. (*b*, right-hand axis) The ratio of the γ-photon number over the sum of electron and positron numbers as a function of a_0 for an electron number density of 10^{23}–10^{24} cm^{-3}.

3.5. *Dependency on the laser power*

As we have shown for an ∼80 PW RP laser, κ_γ is ∼47 % for targets thicker than 2 μm and an electron number density of 1.2×10^{24} cm^{-3}. A consequent question arises as to why the choice of ∼80 PW is made and what is the effect of altering the laser power. To address that topic, the simulations for a RP laser were extended in the power range of 1 PW $\leqslant P \leqslant$ 300 PW, where the electron number density was varying in the range 10^{23} cm^{-3} $\leqslant n_e \leqslant$ 10^{24} cm^{-3}. As per the results of § 3.4, κ_γ varies insignificantly on decreasing the electron number density from 1.2×10^{24} cm^{-3} to 10^{24} cm^{-3}.

Let us consider the case where the electron number density is fixed at 10^{24} cm^{-3} and the laser power varies. The value of κ of each species is shown in figure 5, where $a_0 \approx 307$ for 1 PW, while $a_0 \approx 5318$ for 300 PW. Plots of κ_γ, κ_{e+}, κ_{e-} and κ_{i+} are shown as black, red, blue and green continuous lines, respectively, while the percentage of the laser energy remaining as electromagnetic energy, κ_{EM}, is shown by the purple continuous line.

From the purple line in figure 5 one can observe that at low laser power the laser cannot be efficiently absorbed by the target and it is mostly reflected, since at low power the skin depth does not have significant relativistic increase. However, by increasing the laser power to 20 PW, corresponding to $a_0 \sim 1400$, ∼75 % of the laser energy is absorbed by the target. On further increasing the power up to 300 PW,the percentage of laser energy absorbed increases, although with a lower rate as power increases and eventually saturating at ∼10 %.

At ∼20 PW, κ_γ, κ_{e-} and κ_{i+} become equally important. At $P \lessapprox 5$ PW, most of the laser energy is transferred to electrons and ions, with γ-photons and positrons obtaining an insignificantly low laser energy fraction. However, the picture reverses for $P \gtrapprox 20$ PW, where κ_{i+} saturates at ∼15 %. The value of κ_{e-} also exhibits a plateau region

https://doi.org/10.1017/S0022377821001318 Published online by Cambridge University Press

at 1 PW $\lessapprox P \lessapprox$ 5 PW, after which κ_{e-} continuously decreases for increasing laser power and eventually saturating at ∼10 %. The value of κ_{e+} continuously increases for laser power up to ∼80 PW, where after obtaining a maximum value of ∼9 % it decreases to ∼5 % for higher power values.

The trend of κ_γ in figure 5 changes at a power of ∼80 PW. Since κ_{e+}, κ_{e-} and κ_{i+} all saturate for increasing power, then κ_γ unavoidably also saturates, where the sum of κ_{e+}, κ_{e-} and κ_{i+} suggests a κ_γ saturation at ∼60 %. Therefore, we treat the κ_γ function as the difference of a 'Logistic' and a 'LogNormal' function, given respectively by the left- and right-hand parts of the following equation:

$$\kappa_\gamma = A_2 + \frac{A_1 - A_2}{1 + (x/x_0)^p} + \frac{A_3}{wx}\exp\left\{-\frac{\left[\ln(x/x_c)\right]^2}{2w^2}\right\}. \tag{3.6}$$

The Logistic function is a saturating function representing γ-photon generation. The LogNormal function is an asymmetric peak function which is chosen for γ-photon loss representation due to e^-–e^+ pair generation, since its asymmetric behaviour allows fitting without prior knowledge of the physical loss (or gain) behaviour. Fitting of (3.6) to κ_γ as shown in figure 5(*b*) gives $A_1 \approx -1.75$, $A_2 \approx 59.8$, $p \approx 2.05$, $x_0 \approx 1463$, $A_3 \approx 2213$, $w \approx -0.151$ and $x_c \approx 4088$.

The Logistic function (black dashed line in figure 5*b*) explains the expected κ_γ saturation for an increasing laser power. The parameter A_2 suggests κ_γ saturation at ∼59.8 %, while the parameter A_1 suggests that at an electron number density of 10^{24} cm^{-3} no γ-photons can be produced for a laser power of ∼0.7 PW. The LogNormal function (black dotted line in figure 5*b*), having a negative sign, suggests that a γ-photon population is lost to e^-–e^+ pairs, where their contribution becomes most significant for ∼177 PW as suggested by the parameter x_c.

By repeating the analysis described above for electron number densities in the range 10^{23} cm$^{-3} \leqslant n_e \leqslant 10^{24}$ cm^{-3} we find the optimal electron density value at each power for maximising κ_γ, plotted by the orange line in figure 5(*b*). The trend suggests that 1 PW is sufficient for κ_γ of ∼3 %. The density–power contour suggests that κ_γ is strongly dependent on the electron number density at low laser power, optimal at 2×10^{23} cm^{-3} for a 1 PW laser. By increasing the laser power, denser targets are required to give the peak κ_γ, although the density dependency becomes less prominent as power increases.

The pink line on the right-hand side of figure 5(*b*) shows the ratio of γ-photon number produced to the sum of electron and positron numbers as a function of a_0. The line exhibits an approximately linearly increasing trend, suggesting that at higher laser powers each electron/positron can emit γ-photons several times by the end of the simulation. For an ∼80 PW laser, each electron/positron emits γ-photons approximately three times.

4. Interaction of γ-ray flash with high-Z target

In order to examine the effect of the γ-ray flash described in § 3.3 on a secondary, high-Z target, we perform MC simulations using the FLUKA code (Battistoni *et al.* 2015; Böhlen *et al.* 2014) and its graphical interface FLAIR (Vlachoudis 2009). In addition to γ-photons, the effects of the charged PIC-produced particles on the secondary target are also investigated. The PIC output particles (type, position, momentum and weight) are imported to FLUKA as primary particles. The secondary target is modelled as a 10 mm thick disk of 100 mm in diameter and it is located at 0.1 mm from the focal spot coordinates. The large acceptance angle covered by the secondary target allows one to intercept almost all PIC-generated particles in the forward direction. Natural lead, Pb, is chosen as material for the disk because of its high cross-section for pair production

https://doi.org/10.1017/S0022377821001318 Published online by Cambridge University Press

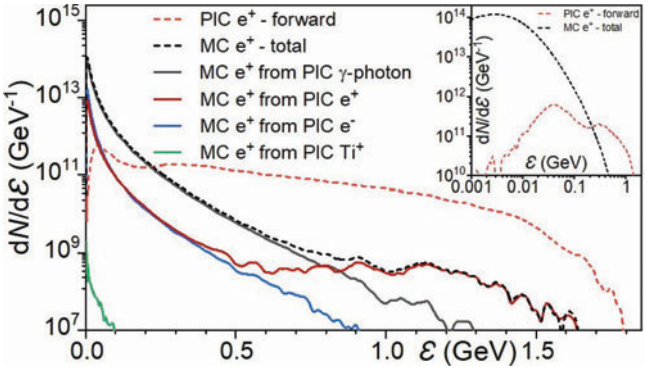

FIGURE 6. For each λ^3 pulse, the energy spectrum of the PIC positrons moving in the forward direction (red dashed), along with the positron spectra from the MC simulations in total (black dashed line) and separated per producing species (γ-photons (black), electrons (blue), positrons (red) and titanium ions (green)).

and photonuclear interactions for energies considered. For the simulations, the FLUKA PRECISIO defaults are used. Additionally, the electromagnetic transport thresholds are set at 0.1 MeV, the photonuclear and electronuclear interactions are enabled, as well as the evaporation of heavy fragments and nuclear coalescence.

Figure 6 shows the PIC-generated positrons moving in the forward direction, exhibiting a rather flat spectrum with a temperature of ∼0.4 GeV. The figure overplots the spectra of positrons escaping the secondary target in the forward direction, obtained from the MC simulations, integrated (black dashed line) and separated per primary particle species (solid lines), namely γ-photons, electrons, positrons and titanium ions. From figure 6 it is seen that the largest number of positrons (∼81.4 %) is produced by γ-photons and that the most energetic positrons are those directly created in the PIC simulations.

Positrons produced by PIC γ-photons and electrons have a temperature of ∼0.1 GeV. The positron population exhibits two temperatures, the first of ∼0.1 GeV corresponding to those generated in the lead target, and the second at higher temperature corresponding to PIC-generated positrons. The low-temperature positrons are generated via e^-–e^+ pair production from Bremsstrahlung γ-photons. The positron spectra after the secondary target areshifted towards lower energy with respect to the PIC-produced positrons, while their total number is increased by approximately an order of magnitude.

Monte Carlo simulations also allow one to estimate the number of stable and unstable nuclides generated in the lead target. Figure 7 shows achart of the produced nuclides focused around the lead position and separated per PIC particle species. Stable nuclides are highlighted with a box. Most of the residual nuclides are produced through photonuclear interactions, either directly by primary (PIC) γ-photons or indirectly by secondary (Bremsstrahlung from fast electrons/positrons) γ-photons. In our γ-photon energy region of interest, the giant dipole resonance photonuclear process dominates since it has the highest integrated cross-section, peaking at ∼13.6 MeV γ-photons. Apart from photonuclear interactions, residual nuclides can be also produced by nucleus–nucleus interactions and/or electronuclear interactions.

One of the most abundant generated lead isotopes is $^{203}_{82}$Pb, where $\sim 10^9$ nuclides are produced with a half-life of ∼52 h. Its direct decay to $^{203}_{81}$Tl (stable) is through electron capture and it does not emit any hadrons. In addition, photons of ∼279.2 keV are emitted which are particularly suitable for medical imaging (Azzam, Said & Al-abyad 2014). The

https://doi.org/10.1017/S0022377821001318 Published online by Cambridge University Press

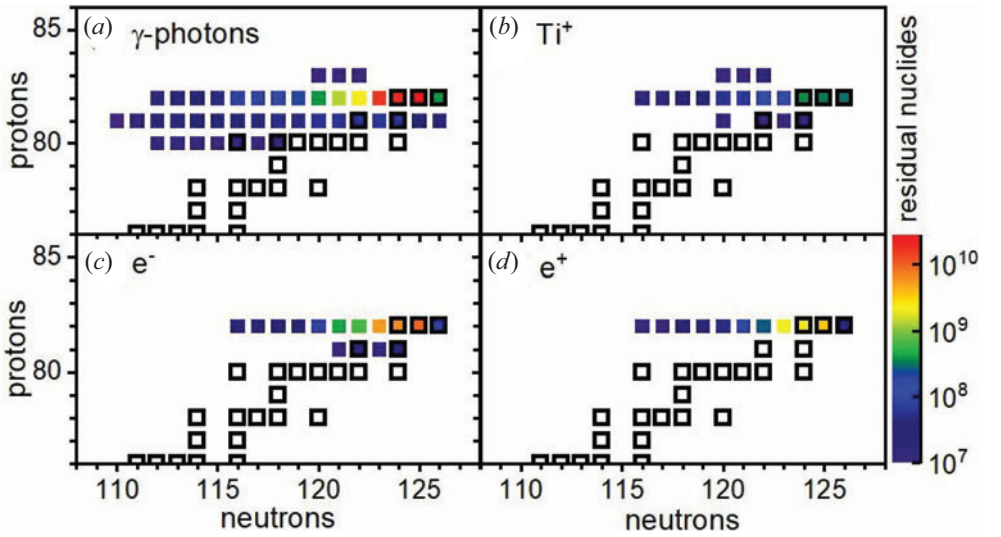

FIGURE 7. Chart of residual nuclides obtained from MC simulation per λ^3 pulse and separated per PIC particle species. Stable nuclides are highlighted with a box.

second most abundant isotope produced is thallium, with $^{201}_{81}$Tl ($\sim 10^8$ nuclides) historically beingused extensively for nuclear medicine (Tadamura *et al.* 1999) due to its decay to $^{201}_{80}$Hg (stable) through electron capture with a half-life of $\sim$73 h.

5. Summary and conclusions

In this work we study highly efficient γ-photon generation through an ultra-intense laser and solid target interaction. We employ the λ^3 regime, where a single-cycle laser pulse ($\sim$80 PW) is focused to a sphere $\sim\lambda/2$ in diameter. The benefit of the λ^3 regime is that it provides the highest intensity achievable at a given laser power, at the expense of the least energy. In this paper we study the interaction of a λ^3 laser with matter in the quantum electrodynamics regime, where copious numbers of γ-photons and e^-–e^+ pairs are generated. The quantum electrodynamics processes are studied by use of the three-dimensional EPOCH PIC code. The λ^3 laser fields are imported into EPOCH after being calculated independently through our developed code.

Our work examines the laser–target interaction for RP, LP and AP lasers. A multi-parametric study is presented, where the variables include the target thickness and electron number density. It is found that the optimal κ_γ reaches $\sim$47 % and it occurs for a RP laser at a target thickness of 2 μm and an electron number density of 1.2×10^{24} cm^{-3}. For the same target parameters, the LP and AP lasers result in κ_γ of $\sim$40 % and $\sim$20 %, respectively. For the optimal target variables, the LP laser gives κ_γ of $\sim$42 %, while the AP laser gives κ_γ of $\sim$29 %.

The significantly higher κ_γ for the RP laser is due to the dominance of the longitudinal, E_x, field that increases the coupling of the laser to the target. For the LP laser E_x is smaller, while for the AP laser it is absent. The E_x field assists in the formation of a target cavity, where the cavity propagation performs a different propagation depending on the laser polarisation mode. Interference of the reflected/diffracted laser field inside the cavity results in an instantaneous intensity as high as $\sim 8.8 \times 10^{25}$ W cm^{-2}, approximately one order of magnitude higher than the intensity expected on focus.

https://doi.org/10.1017/S0022377821001318 Published online by Cambridge University Press

The directionality of electrons at several instances is identified, resulting in several high-energy electron groups directed at $\sim 0^\circ$, $\sim 180^\circ$ and $\sim 60^\circ$ for a RP laser. Those electrons are connected to the γ-photon directionality, being at the same angles. The ultra-high intensities employed result in not only prolific γ-photon generation but unavoidably also e^-–e^+ pair generation through the multi-photon Breit–Wheeler process. The generation positions of e^-–e^+ pairs is identified to overlap the regions of high-energy γ-photons.

At a time of $\sim\lambda/(2c)$ after the peak of the laser pulse reaches the focal spot, the γ-photons expand radially in a ballistic fashion without significant losses to e^-–e^+pairs. The γ-photons expand within a spherical shell where the FWHM of their energy density is approximately equal to the laser wavelength, similar to the laser–foil interaction time. The expanding spherical shell for the RP, LP and AP lasers results in a γ-ray flash of ~ 31, ~ 28 and ~ 13 PW, respectively. Although a preferred directionality exists for the γ-photons, the radiant intensity of the population at $\sim 60^\circ$ is less significant due to its large solid angle, in contrast to γ-photons at $\sim 0^\circ$ and $\sim 180^\circ$.

Our analysis is also extended to varying the laser power in the range 1 PW $\leqslant P \leqslant$ 300 PW. We demonstrate that κ_γ sharply increases up to ~ 80 PW, while γ-photons become the dominant species above ~ 20 PW. For low laser powers, there is a strong dependency of κ_γ on the electron number density, where the optimal electron number density increases approximately linearly with a_0. For higher power values this dependency becomes less important. When increasing the laser power then κ_γ increases, saturating at $\sim 60\,\%$. A κ_γ discontinuity exists centred at ~ 177 PW, attributed to the γ-photon conversion to e^-–e^+ pairs, while as power further increases the γ-photon reduction is compensated by further γ-photon emission by positrons, in the same manner as by electrons. In addition, as laser power increases then the number of γ-photons emitted from each electron/positron also increases in an approximately linear fashion with a_0.

Finally, for the RP laser, the interaction of the PIC-generated particles interacting with a high-Z target is studied by MC simulations. The spectra of each particle species escaping the secondary target are obtained. The PIC spectra are substantially altered by the interaction with the high-Z target. The γ-ray flash interaction with the secondary target also results in significant production of radioactive nuclides, whose yields are estimated. Hence, the coupling of PIC and MC simulations provides a powerful tool for further investigating the interaction of lasers with matter.

Supplementary movie

Supplementary movie is available at https://doi.org/10.1017/S0022377821001318.

Acknowledgements

The authors would like to acknowledge useful communication with Dr D. Khikhlukha and K. Lezhnin. This work is supported by the projects High Field Initiative (CZ.02.1.01/0.0/0.0/15_003/0000449) from the European Regional Development Fund and ‘e-INFRA CZ’ (ID:90140) from the Ministry of Education, Youth and Sports of the Czech Republic. C.P.R. would like to acknowledge funding from EPSRC, grant no. EP/V049461/1. The EPOCH code is in part funded by UK EPSRC grants EP/G054950/1, EP/G056803/1, EP/G055165/1 and EP/M022463/1.

Editor Luís O. Silva thanks the referees for their advice in evaluating this article.

Declaration of interests

The authors report no conflict of interest.

Appendix A

This appendix gives the imaginary part of the integrands used for the electric and magnetic field calculation (Jeong *et al.* 2015) of a LP laser, as used in our Fortran code. The definition of symbols is found in § 2.1. The electric field integrands are

$$I_{Ex-L} = -A^2 B\cos(\phi)X\cos(F) + [A^2\cos(\phi) - A^2\cos(\phi)X]\sin(F), \tag{A 1}$$

$$I_{Ey-L} = -A^2 B\cos(\phi)Y\cos(F) + [A - A^2\cos(\phi)Y]\sin(F), \tag{A 2}$$

$$I_{Ez-L} = -A^2 B\cos(\phi)Z\cos(F) - [A^2\cos(\phi)Z]\sin(F). \tag{A 3}$$

The magnetic field integrands are

$$I_{Bx-L} = ABZ\cos(F) + AZ\sin(F), \tag{A 4}$$

$$I_{By-L} = -A^2 B\cos(\phi)Z\cos(F) - [A^2\cos(\phi)Z]\sin(F), \tag{A 5}$$

$$I_{Bz-L} = [A^2 B\cos(\phi)Y - ABX]\cos(F) + [A^2\cos(\phi)Y - AX]\sin(F). \tag{A 6}$$

Appendix B

This appendix gives the imaginary part of the integrands used for the electric and magnetic field calculation (Jeong *et al.* 2018) of a RP laser, as used in our Fortran code. The definition of symbols is found in § 2.1. The electric field integrands are

$$I_{Ex-R} = A^2 BX\sin(F) - [A^2 X - A^2]\cos(F), \tag{B 1}$$

$$I_{Ey-R} = A^2 BY\sin(F) - [A^2 Y - A\cos(\phi)]\cos(F), \tag{B 2}$$

$$I_{Ez-R} = A^2 BZ\sin(F) - [A^2 Z - A\sin(\phi)]\cos(F). \tag{B 3}$$

The magnetic field integrands are

$$I_{Bx-R} = 0, \tag{B 4}$$

$$I_{By-R} = A[\sin(\phi)X - AZ]\cos(F) - AB[\sin(\phi)X - AZ]\sin(F), \tag{B 5}$$

$$I_{Bz-R} = -A[\cos(\phi)X - AY]\cos(F) + AB[\cos(\phi)X - AY]\sin(F). \tag{B 6}$$

REFERENCES

1998 Accelerator driven systems:energy generation and transmutation of nuclear waste: status report. TECDOC Series 985. International Atomic Energy Agency.

Aharonian, F., An, Q., Axikegu, Bai, L.X., Bai, Y.X., Bao, Y.W., Bastieri, D., Bi, X.J., Bi, Y.J., Cai, H., *et al.* 2021 Extended very-high-energy gamma-ray emission surrounding PSR J0622 + 3749 observed by LHAASO-KM2A. *Phys. Rev. Lett.* **126**, 241103.

Aichelin, J. 1991 Quantum molecular dynamics—a dynamical microscopic n-body approach to investigate fragment formation and the nuclear equation of state in heavy ion collisions. *Phys. Rep.* **202** (5), 233–360.

April, A. & Piché, M. 2010 4π focusing of TM01 beams under nonparaxial conditions. *Opt. Express* **18** (21), 22128–22140.

Arber, T.D., Bennett, K., Brady, C.S., Lawrence-Douglas, A., Ramsay, M.G., Sircombe, N.J., Gillies, P., Evans, R.G., Schmitz, H., Bell, A.R., *et al.* 2015 Contemporary particle-in-cell approach to laser-plasma modelling. *Plasma Phys. Control. Fusion* **57** (11), 113001.

Audet, T.L., Alejo, A., Calvin, L., Cunningham, M.H., Frazer, G.R., Nersisyan, G., Phipps, M. L, Warwick, J.R., Sarri, G., Hafz, N.A.M., *et al.* 2021 Ultrashort, MeV-scale laser-plasma positron source for positron annihilation lifetime spectroscopy. *Phys. Rev. Accel. Beams* **24**, 073402.

https://doi.org/10.1017/S0022377821001318 Published online by Cambridge University Press

AZZAM, A., SAID, S.A. & AL-ABYAD, M. 2014 Evaluation of different production routes for the radio medical isotope ^{203}Pb using TALYS 1.4 and EMPIRE 3.1 code calculations. *Appl. Radiat. Isot*. **91**, 109–113.

BAHK, S.W., ROUSSEAU, P., PLANCHON, T.A., CHVYKOV, V., KALINTCHENKO, G., MAKSIMCHUK, A., MOUROU, G.A. & YANOVSKY, V. 2004 Generation and characterization of the highest laser intensities (10^{22} W/cm^2). *Opt. Lett*. **29** (24), 2837–2839.

BATTISTONI, G., BOEHLEN, T., CERUTTI, F., CHIN, P.W., ESPOSITO, L.S., FASSÒ, A., FERRARI, A., LECHNER, A., EMPL, A., MAIRANI, A., *et al.* 2015 Overview of the FLUKA code. *Ann. Nucl. Energy* **82**, 10–18.

BELL, A.R. & KIRK, J.G. 2008 Possibility of prolific pair production with high-power lasers. *Phys. Rev. Lett*. **101**, 200403.

BERESTETSKII, V.B., LIFSHITZ, E.M. & PITAEVSKII, L.P. 1982 *Quantum Electrodynamics*, 2d edn. Butterworth-Heinemann.

BETHE, H. & HEITLER, W. 1934 On the stopping of fast particles and on the creation of positive electrons. *Proc. R. Soc. Lond.* A **146** (856), 83–112.

BÖHLE, F., KRETSCHMAR, M., JULLIEN, A., KOVACS, M., MIRANDA, M., ROMERO, R., CRESPO, H., MORGNER, U., SIMON, P., LOPEZ-MARTENS, R., *et al.* 2014 Compression of CEP-stable multi-mJ laser pulses down to 4 fs in long hollow fibers. *Laser Phys. Lett*. **11** (9), 095401.

BÖHLEN, T.T., CERUTTI, F., CHIN, M.P.W., FASSÒ, A., FERRARI, A., ORTEGA, P.G., MAIRANI, A., SALA, P.R., SMIRNOV, G. & VLACHOUDIS, V. 2014 The FLUKA code: developments and challenges for high energy and medical applications. *Nucl. Data Sheets* **120**, 211–214.

BORIS, J.P. 1970 Relativistic plasma simulation-optimization of a hybrid code. In *Proceedings of Fourth Conference on Numerical Simulations of Plasmas* (eds. J.P. Boris & R.A. Shanny), pp. 3–67. Naval Research Laboratory.

BORN, M. & WOLF, E. 1964 *Principles of Optics: Electromagnetic Theory of Propagation, Interference and Diffraction of Light*, 2nd edn. Pergamon.

BRABEC, T. & KRAUSZ, F. 2000 Intense few-cycle laser fields: frontiers of nonlinear optics. *Rev. Mod. Phys*. **72**, 545–591.

BUDNEV, V.M., GINZBURG, I.F., MELEDIN, G.V. & SERBO, V.G. 1975 The two-photon particle production mechanism. Physical problems. Applications. Equivalent photon approximation. *Phys. Rep*. **15** (4), 181–282.

BULANOV, S.S., ESAREY, E., SCHROEDER, C.B., BULANOV, S.V., ESIRKEPOV, T.Z., KANDO, M., PEGORARO, F. & LEEMANS, W.P. 2016 Radiation pressure acceleration: the factors limiting maximum attainable ion energy. *Phys. Plasmas* **23** (5), 056703.

BULANOV, S.S., ESIRKEPOV, T.Z., KAMENETS, F.F. & PEGORARO, F. 2006 Single-cycle high-intensity electromagnetic pulse generation in the interaction of a plasma wakefield with regular nonlinear structures. *Phys. Rev.* E **73**, 036408.

BULANOV, S.V., ESIRKEPOV, T.Z., KANDO, M., KOGA, J., KONDO, K. & KORN, G. 2015 On the problems of relativistic laboratory astrophysics and fundamental physics with super powerful lasers. *Plasma Phys. Rep*. **41**, 1–51.

CARDENAS, D.E., OSTERMAYR, T.M., DI LUCCHIO, L., HOFMANN, L., KLING, M.F., GIBBON, P., SCHREIBER, J. & VEISZ, L. 2019 Sub-cycle dynamics in relativistic nanoplasma acceleration. *Sci. Rep*. **9**, 7321.

CHEN, H., MEYERHOFER, D.D., WILKS, S.C., CAUBLE, R., DOLLAR, F., FALK, K., GREGORI, G., HAZIM, A., MOSES, E.I., MURPHY, C.D., *et al.* 2011 Towards laboratory produced relativistic electron-positron pair plasmas. *High Energy Density Phys*. **7** (4), 225–229.

CHENG, Z., ZHOU, Y., XIA, M., LI, W., YANG, K. & ZHOU, Y. 2015 Tight focusing of the azimuthally polarized light beam for a sharper spot. *Opt. Laser Technol*. **73**, 77–81.

COMPTON, A.H. 1923 A quantum theory of the scattering of X-rays by light elements. *Phys. Rev*. **21**, 483–502.

DANSON, C.N., HAEFNER, C., BROMAGE, J., BUTCHER, T., CHANTELOUP, J.F., CHOWDHURY, E.A., GALVANAUSKAS, A., GIZZI, L.A., HEIN, J., HILLIER, D.I., *et al.* 2019 Petawatt and exawatt class lasers worldwide. *High Power Laser Sci*. **7**, e54.

DORN, R., QUABIS, S. & LEUCHS, G. 2003 Sharper focus for a radially polarized light beam. *Phys. Rev. Lett*. **91**, 233901.

EHLOTZKY, F., KRAJEWSKA, K. & KAMIŃSKI, J.Z. 2009 Fundamental processes of quantum electrodynamics in laser fields of relativistic power. *Rep. Prog. Phys*. **72** (4), 046401.

ELIASSON, B. & LIU, C.S. 2013 An electromagnetic gamma-ray free electron laser. *J. Plasma Phys*. **79** (6), 995–998.

ESIRKEPOV, T.Z., BORGHESI, M., BULANOV, S.V., MOUROU, G. & TAJIMA, T. 2004 Highly efficient relativistic-ion generation in the laser-piston regime. *Phys. Rev. Lett*. **92**, 175003.

GHOTRA, H.S. & KANT, N. 2015 Sensitiveness of axial magnetic field on electron acceleration by a radially polarized laser pulse in vacuum. *Opt. Commun*. **356**, 118–122.

GONG, Z., HU, R.H., SHOU, Y.R., QIAO, B., CHEN, C.E., HE, X.T., BULANOV, S.S., ESIRKEPOV, T.ZH., BULANOV, S.V. & YAN, X.Q. 2017 High-efficiency γ-ray flash generation via multiple-laser scattering in ponderomotive potential well. *Phys. Rev.* E **95**, 013210.

GRISMAYER, T., VRANIC, M., MARTINS, J.L., FONSECA, R.A. & SILVA, L.O. 2016 Laser absorption via quantum electrodynamics cascades in counter propagating laser pulses. *Phys. Plasmas* **23** (5), 056706.

GU, Y.J., KLIMO, O., BULANOV, S.V. & WEBER, S. 2018 Brilliant gamma-ray beam and electron-positron pair production by enhanced attosecond pulses. *Commun. Phys*. **1**, 1–9.

HADJISOLOMOU, P., JEONG, T.M., VALENTA, P., KORN, G. & BULANOV, S.V. 2021 Gamma-ray flash generation in irradiating a thin foil target by a single-cycle tightly focused extreme power laser pulse. *Phys. Rev.* E **104**, 015203.

HAYWARD, E. 1970 *Photonuclear Reactions*. National Bureau of Standards.

HIGUERA, A.V. & CARY, J.R. 2017 Structure-preserving second-order integration of relativistic charged particle trajectories in electromagnetic fields. *Phys. Plasmas* **24** (5), 052104.

ILDERTON, A. 2019 Note on the conjectured breakdown of QED perturbation theory in strong fields. *Phys. Rev.* D **99**, 085002.

JEONG, T.M., BULANOV, S.V., WEBER, S. & KORN, G. 2018 Analysis on the longitudinal field strength formed by tightly-focused radially-polarized femtosecond petawatt laser pulse. *Opt. Express* **26** (25), 33091–33107.

JEONG, T.M., WEBER, S., LE GARREC, B., MARGARONE, D., MOCEK, T. & KORN, G. 2015 Spatio-temporal modification of femtosecond focal spot under tight focusing condition. *Opt. Express* **23** (9), 11641–11656.

JI, L.L., SNYDER, J. & SHEN, B.F. 2019 Single-pulse laser-electron collision within a micro-channel plasma target. *Plasma Phys. Control. Fusion* **61** (6), 065019.

KIRK, J.G., BELL, A.R. & ARKA, I. 2009 Pair production in counter-propagating laser beams. *Plasma Phys. Control. Fusion* **51** (8), 085008.

KLIMO, O., PSIKAL, J., LIMPOUCH, J. & TIKHONCHUK, V.T. 2008 Monoenergetic ion beams from ultrathin foils irradiated by ultrahigh-contrast circularly polarized laser pulses. *Phys. Rev. ST Accel. Beams* **11**, 031301.

KOCH, H.W. & MOTZ, J.W. 1959 Bremsstrahlung cross-section formulas and related data. *Rev. Mod. Phys*. **31**, 920–955.

KOGA, J., ESIRKEPOV, T.Z. & BULANOV, S.V. 2005 Nonlinear Thomson scattering in the strong radiation damping regime. *Phys. Plasmas* **12** (9), 093106.

LANDAU, L. 1944 On the energy loss of fast particles by ionization. *J. Phys. USSR* **8** (1–6), 201–205.

LEZHNIN, K.V., SASOROV, P.V., KORN, G. & BULANOV, S.V. 2018 High power gamma flare generation in multi-petawatt laser interaction with tailored targets. *Phys. Plasmas* **25** (12), 123105.

LI, J.X., SALAMIN, Y.I., GALOW, B.J. & KEITEL, C.H. 2012 Acceleration of proton bunches by petawatt chirped radially polarized laser pulses. *Phys. Rev.* A **85**, 063832.

LI, Z., KATO, Y. & KAWANAKA, J. 2021 Simulating an ultra-broadband concept for Exawatt-class lasers. *Sci. Rep*. **11** (151), 1–16.

LUO, W., ZHU, Y.B., ZHUO, H.B., MA, Y.Y., SONG, Y.M., ZHU, Z.C., WANG, X.D., LI, X.H., TURCU, I.C.E. & CHEN, M. 2015 Dense electron-positron plasmas and gamma-ray bursts generation by counter-propagating quantum electrodynamics-strong laser interaction with solid targets. *Phys. Plasmas* **22** (6), 063112.

MAGNUSSON, J., GONOSKOV, A., MARKLUND, M., ESIRKEPOV, T.Z., KOGA, J.K., KONDO, K., KANDO, M., BULANOV, S.V., KORN, G. & BULANOV, S.S. 2019 Laser-particle collider for multi-GeV photon production. *Phys. Rev. Lett*. **122**, 254801.

MOUROU, G., CHANG, Z., MAKSIMCHUK, A., NEES, J., BULANOV, S.V., BYCHENKOV, V.Y., ESIRKEPOV, T.Z., NAUMOVA, N.M., PEGORARO, F. & RUHL, H. 2002 On the design of experiments for the study of relativistic nonlinear optics in the limit of single-cycle pulse duration and single-wavelength spot size. *Plasma Phys. Rep*. **28**, 12–27.

MOUROU, G., MIRONOV, S., KHAZANOV, E. & SERGEEV, A. 2014 Single cycle thin film compressor opening the door to Zeptosecond–Exawatt physics. *Eur. Phys. J. Spec. Top*. **223**, 1181–1188.

MOUROU, G.A., TAJIMA, T. & BULANOV, S.V. 2006 Optics in the relativistic regime. *Rev. Mod. Phys*. **78**, 309–371.

NAKAMURA, T., KOGA, J.K., ESIRKEPOV, T.Z., KANDO, M., KORN, G. & BULANOV, S.V. 2012 High-power γ-ray flash generation in ultraintense laser-plasma interactions. *Phys. Rev. Lett*. **108**, 195001.

NAROZHNY, N.B. 1979 Radiation corrections to quantum processes in an intense electromagnetic field. *Phys. Rev.* D **20**, 1313–1320.

NEDOREZOV, V.G., TURINGE, A.A. & SHATUNOV, Y.M. 2004 Photonuclear experiments with Compton-backscattered gamma beams. *Phys.-Usp*. **47** (4), 341–358.

OSVAY, K., BÖRZSÖNYI, A., CAO, H., CORMIER, E., CSONTOS, J., JÓJÁRT, P., KALASHNIKOV, M., KISS, B., LÓPEZ-MARTENS, R., TÓTH, S., *et al.* 2019 Development status and operation experiences of the few cycle high average power lasers of ELI-ALPS (Conference Presentation). In *Short-pulse High-energy Lasers and Ultrafast Optical Technologies* (ed. P. Bakule & C.L. Haefner), vol. 11034. International Society for Optics and Photonics, SPIE.

OUILLÉ, M., VERNIER, A., BÖHLE, F., BOCOUM, M., JULLIEN, A., LOZANO, M., ROUSSEAU, J.P., CHENG, Z., GUSTAS, D., BLUMENSTEIN, A., *et al.* 2020 Relativistic-intensity near-single-cycle light waveforms at kHz repetition rate. *Light Sci. Appl*. **9**, 1–9.

PAYEUR, S., FOURMAUX, S., SCHMIDT, B.E., MACLEAN, J.P., TCHERVENKOV, C., LÉGARÉ, F., PICHÉ, M. & KIEFFER, J.C. 2012 Generation of a beam of fast electrons by tightly focusing a radially polarized ultrashort laser pulse. *Appl. Phys. Lett*. **101** (4), 041105.

PERRY, M.D., PENNINGTON, D., STUART, B.C., TIETBOHL, G., BRITTEN, J.A., BROWN, C., HERMAN, S., GOLICK, B., KARTZ, M., MILLER, J., *et al.* 1999 Petawatt laser pulses. *Opt. Lett*. **24** (3), 160–162.

PHILIPPOV, A.A. & SPITKOVSKY, A. 2018 Ab-initio pulsar magnetosphere: particle acceleration in oblique rotators and high-energy emission modeling. *Astrophys. J*. **855** (2), 94.

PIROZHKOV, A.S., FUKUDA, Y., NISHIUCHI, M., KIRIYAMA, H., SAGISAKA, A., OGURA, K., MORI, M., KISHIMOTO, M., SAKAKI, H., DOVER, N.P., *et al.* 2017 Approaching the diffraction-limited, bandwidth-limited Petawatt. *Opt. Express* **25** (17), 20486–20501.

PODSZUS, T. & DI PIAZZA, A. 2019 High-energy behavior of strong-field QED in an intense plane wave. *Phys. Rev.* D **99**, 076004.

REES, M.J. & MÉSZÁROS, P. 1992 Relativistic fireballs: energy conversion and time-scales. *Mon. Not. R. Astron. Soc*. **258** (1), 41P–43P.

RICHARDS, B., WOLF, E. & GABOR, D. 1959 Electromagnetic diffraction in optical systems, II. Structure of the image field in an aplanatic system. *Proc. R. Soc. Lond.* A **253** (1274), 358–379.

RIDGERS, C.P., BRADY, C.S., DUCLOUS, R., KIRK, J.G., BENNETT, K., ARBER, T.D. & BELL, A.R. 2013 Dense electron-positron plasmas and bursts of gamma-rays from laser-generated quantum electrodynamic plasmas. *Phys. Plasmas* **20** (5), 056701.

RIDGERS, C.P., BRADY, C.S., DUCLOUS, R., KIRK, J.G., BENNETT, K., ARBER, T.D., ROBINSON, A.P.L. & BELL, A.R. 2012 Dense electron-positron plasmas and ultraintense γ rays from laser-irradiated solids. *Phys. Rev. Lett*. **108**, 165006.

RIDGERS, C.P., KIRK, J.G., DUCLOUS, R., BLACKBURN, T.G., BRADY, C.S., BENNETT, K., ARBER, T.D. & BELL, A.R. 2014 Modelling gamma-ray photon emission and pair production in high-intensity laser-matter interactions. *J. Comput. Phys*. **260**, 273–285.

RITUS, V.I. 1970 Radiative effects and their enhancement in an intense electromagnetic field. *J. Expl Theor. Phys*. **30** (6), 1181.

https://doi.org/10.1017/S0022377821001318 Published online by Cambridge University Press

RIVAS, D.E., BOROT, A., CARDENAS, D.E., MARCUS, G., GU, X., HERRMANN, D., XU, J., TAN, J., KORMIN, D., MA, G., *et al.* 2017 Next generation driver for attosecond and laser-plasma physics. *Sci. Rep*. **7**, 1–8.

ROBINSON, A.P.L., ZEPF, M., KAR, S., EVANS, R.G. & BELLEI, C. 2008 Radiation pressure acceleration of thin foils with circularly polarized laser pulses. *New J. Phys*. **10** (1), 013021.

SALAMIN, Y.I. 2006 Fields of a radially polarized Gaussian laser beam beyond the paraxial approximation. *Opt. Lett*. **31** (17), 2619–2621.

SALAMIN, Y.I. 2010*a* Direct particle acceleration by two identical crossed radially polarized laser beams. *Phys. Rev.* A **82**, 013823.

SALAMIN, Y.I. 2010*b* Low-diffraction direct particle acceleration by a radially polarized laser beam. *Phys. Lett.* A **374** (48), 4950–4953.

SALAMIN, Y.I. 2015 Fields and propagation characteristics in vacuum of an ultrashort tightly focused radially polarized laser pulse. *Phys. Rev.* A **92**, 053836.

SALES, T.R.M. 1998 Smallest focal spot. *Phys. Rev. Lett*. **81**, 3844–3847.

SARRI, G., PODER, K., COLE, J.M., SCHUMAKER, W., DI PIAZZA, A., REVILLE, B., DZELZAINIS, T., DORIA, D., GIZZI, L.A., GRITTANI, G., *et al.* 2015 Generation of neutral and high-density electron–positron pair plasmas in the laboratory. *Nat. Commun*. **6** (6747), 1–8.

SCHNEIDER, U., AGOSTEO, S., PEDRONI, E. & BESSERER, J. 2002 Secondary neutron dose during proton therapy using spot scanning. *Intl J. Radiat. Oncol. Biol. Phys*. **53** (1), 244–251.

STARK, D.J., TONCIAN, T. & AREFIEV, A.V. 2016 Enhanced multi-MeV photon emission by a laser-driven electron beam in a self-generated magnetic field. *Phys. Rev. Lett*. **116**, 185003.

STRICKLAND, D. & MOUROU, G. 1985 Compression of amplified chirped optical pulses. *Opt. Commun*. **56** (3), 219–221.

TADAMURA, E., KUDOH, T., MOTOOKA, M., INUBUSHI, M., SHIRAKAWA, S., HATTORI, N., OKADA, T., MATSUDA, T., KOSHIJI, T., NISHIMURA, K., *et al.* 1999 Assessment of regional and global left ventricular function by reinjection Tl-201 and rest Tc-99m sestamibi ECG-gated SPECT: Comparison with three-dimensional magnetic resonance imaging. *J. Am. Coll. Cardiol*. **33** (4), 991–997.

TAMBURINI, M., DI PIAZZA, A., LISEYKINA, T.V. & KEITEL, C.H. 2014*a* Plasma-based generation and control of a single few-cycle high-energy ultrahigh-intensity laser pulse. *Phys. Rev. Lett*. **113**, 025005.

TAMBURINI, M., KEITEL, C.H. & DI PIAZZA, A. 2014*b* Electron dynamics controlled via self-interaction. *Phys. Rev.* E **89**, 021201.

TAMBURINI, M., LISEYKINA, T.V., PEGORARO, F. & MACCHI, A. 2012 Radiation-pressure-dominant acceleration: polarization and radiation reaction effects and energy increase in three-dimensional simulations. *Phys. Rev.* E **85**, 016407.

TANAKA, K.A., SPOHR, K.M., BALABANSKI, D.L., BALASCUTA, S., CAPPONI, L., CERNAIANU, M.O., CUCIUC, M., CUCOANES, A., DANCUS, I., DHAL, A., *et al.* 2020 Current status and highlights of the ELI-NP research program. *Matter Radiat. at Extremes* **5** (2), 024402.

VLACHOUDIS, V. 2009 FLAIR: a powerful but user friendly graphical interface for FLUKA. In *Proceedings of the International Conference on Mathematics, Computational Methods & Reactor Physics (M&C 2009), Saratoga Springs, New York*, vol. 176. American Nuclear Society.

VORONIN, A.A., ZHELTIKOV, A.M., DITMIRE, T., RUS, B. & KORN, G. 2013 Subexawatt few-cycle lightwave generation via multipetawatt pulse compression. *Opt. Commun*. **291**, 299–303.

VRANIC, M., GRISMAYER, T., FONSECA, R.A. & SILVA, L.O. 2016 Electron–positron cascades in multiple-laser optical traps. *Plasma Phys. Control. Fusion* **59** (1), 014040.

VSHIVKOV, V.A., NAUMOVA, N.M., PEGORARO, F. & BULANOV, S.V. 1998 Nonlinear electrodynamics of the interaction of ultra-intense laser pulses with a thin foil. *Phys. Plasmas* **5** (7), 2727–2741.

WANG, P.X., HO, Y.K., YUAN, X.Q., KONG, Q., CAO, N., SESSLER, A.M., ESAREY, E. & NISHIDA, Y. 2001 Vacuum electron acceleration by an intense laser. *Appl. Phys. Lett*. **78** (15), 2253–2255.

WANG, T., RIBEYRE, X., GONG, Z., JANSEN, O., D'HUMIÈRES, E., STUTMAN, D., TONCIAN, T. & AREFIEV, A. 2020*a* Power scaling for collimated γ-ray beams generated by structured laser-irradiated targets and its application to two-photon pair production. *Phys. Rev. Appl*. **13**, 054024.

https://doi.org/10.1017/S0022377821001318 Published online by Cambridge University Press

WANG, X.B., HU, G.Y., ZHANG, Z.M., GU, Y.Q., ZHAO, B., ZUO, Y. & ZHENG, J. 2020*b* Gamma-ray generation from ultraintense laser-irradiated solid targets with preplasma. *High Power Laser Sci. Engng* **8**, e34.

WEST, D. 1982 *Ternary Equilibrium Diagrams*. Springer.

WHEELER, J.A. & LAMB, W.E. JR. 1939 Influence of atomic electrons on radiation and pair production. *Phys. Rev*. **55** (9), 858.

YOON, J.W., KIM, Y.G., CHOI, I.W., SUNG, J.H., LEE, H.W., LEE, S.K. & NAM, C.H. 2021 Realization of laser intensity over 10^{23} W/cm^2. *Optica* **8** (5), 630–635.

YOUNIS, A.H., DAVIDSON, A., HAFIZI, B. & GORDON, D.F. 2021 Diagnostic techniques for particle-in-cell simulations of laser-produced gamma-rays in the strong-field QED regime. arXiv: 2106.16227.

ZHANG, L.Q., WU, S.D., HUANG, H.R., LAN, H.Y., LIU, W.Y., WU, Y.C., YANG, Y., ZHAO, Z.Q., ZHU, C.H. & LUO, W. 2021 Brilliant attosecond γ-ray emission and high-yield positron production from intense laser-irradiated nano-micro array. *Phys. Plasmas* **28** (2), 023110.

ZHIDKOV, A., KOGA, J., SASAKI, A. & UESAKA, M. 2002 Radiation damping effects on the interaction of ultraintense laser pulses with an overdense plasma. *Phys. Rev. Lett*. **88**, 185002.

https://doi.org/10.1017/S0022377821001318 Published online by Cambridge University Press